© 2022. Published by The Company of Biologists Ltd | Development (2022) 149, dev199637. doi:10.1242/dev.199637

STEM CELLS AND REGENERATION

TECHNIQUES AND RESOURCES ARTICLE

A constitutively expressed fluorescent ubiquitination-based cell-cycle indicator (FUCCI) in axolotls for studying tissue regeneration

Timothy J. Duerr[1], Eun Kyung Jeon[1], Kaylee M. Wells[2], Antonio Villanueva[1], Ashley W. Seifert[3], Catherine D. McCusker[2] and James R. Monaghan[1,*]

ABSTRACT

Regulation of cell cycle progression is essential for cell proliferation during regeneration following injury. After appendage amputation, the axolotl (*Ambystoma mexicanum*) regenerates missing structures through an accumulation of proliferating cells known as the blastema. To study cell division during blastema growth, we generated a transgenic line of axolotls that ubiquitously expresses a bicistronic version of the fluorescent ubiquitination-based cell-cycle indicator (FUCCI). We demonstrate near-ubiquitous FUCCI expression in developing and adult tissues, and validate these expression patterns with DNA synthesis and mitosis phase markers. We demonstrate the utility of FUCCI for live and whole-mount imaging, showing the predominantly local contribution of cells during limb and tail regeneration. We also show that spinal cord amputation results in increased proliferation at least 5 mm from the site of injury. Finally, we use multimodal staining to provide cell type information for cycling cells by combining fluorescence *in situ* hybridization, EdU click-chemistry and immunohistochemistry on a single FUCCI tissue section. This new line of animals will be useful for studying cell cycle dynamics using *in situ* endpoint assays and *in vivo* imaging in developing and regenerating animals.

KEY WORDS: Regeneration, FUCCI, Cell cycle, Axolotl

INTRODUCTION

Vertebrate tissue regeneration inherently requires cell proliferation either through endogenous stem cell proliferation or re-entry of differentiated cells into the cell cycle. One of the most striking examples of vertebrate regeneration is epimorphic replacement of the amputated salamander appendage. Appendage regeneration requires the generation of a highly proliferative mass of cells called the blastema. The formation of the blastema is dependent on an intact nerve supply and a specialized layer of epithelium known as the apical epithelial cap (AEC) (McCusker et al., 2015a). The AEC likely has multiple functions, including directing outgrowth, maintaining proliferation and secreting factors that allow for remodeling of the underlying extracellular matrix (Stocum, 2017; Tsai et al., 2020). Although the blastema consists of numerous cell types, most cells originate from mesenchymal cell populations located near the amputation plane (Butler, 1933; Currie et al., 2016). Understanding the mechanisms that initiate and sustain proliferation of blastema cells is a fundamental problem that requires modern molecular tools to track and characterize blastema cell behavior (Stocum, 2017; Tanaka, 2016). Although recent developments in transgenesis and tissue grafting techniques have allowed the observation of blastema cells *in vivo* (Currie et al., 2016; Khattak et al., 2013; Kragl and Tanaka, 2009; Sandoval-Guzmán et al., 2014), further development of transgenic lines are needed to enable imaging of the regeneration process.

In 2008, Sakaue-Sawano and colleagues developed the fluorescent, ubiquitination-based cell-cycle indicator (FUCCI) system to study cell cycle progression in human cell lines and mice (Sakaue-Sawano et al., 2008). Since then, several variations have been made to the FUCCI construct, and it has been used to generate transgenic plants (Yin et al., 2014) and animals (Abe et al., 2013; Sugiyama et al., 2009; Zielke et al., 2014). The FUCCI system is based upon the inverse oscillation of Geminin and Cdt1 proteins that occur naturally during the cell cycle (Nishitani et al., 2004). The FUCCI construct includes a constitutively active promoter that drives expression of a fluorescent protein fused to the Cdt1 protein degron, which has high levels in G1 phase due to ubiquitin-mediated proteolysis during S, G2 and early mitotic phases (S/G2/M). Conversely, the Geminin protein degron is fused to a different fluorescent molecule that is degraded during late M and G1, leading to high fluorescent protein levels in S/G2/early M (see Zielke and Edgar, 2015 for a review). Fusion of these two expression cassettes into a single bicistronic transgene allows visualization of cells while they progress through the cell cycle (Bouldin and Kimelman, 2014). In this study, we use a ubiquitously expressed bicistronic FUCCI construct to generate a transgenic line of axolotl salamanders to study cell cycle dynamics during development, limb regeneration and tail regeneration.

RESULTS

Generation and characterization of developing FUCCI axolotls

We chose to design a bicistronic version of the original FUCCI construct because it should theoretically lead to equimolar levels of probes and only require the generation of a single transgenic animal line (Rajan et al., 2018). The construct includes a CAG promoter that drives expression of monomeric Azami-Green fused to the zebrafish geminin degron (mAG-zGem) followed by a viral 2A self-cleaving peptide and mCherry fused to the zebrafish Cdt1 degron (mCherry-zCdt1), which was cloned into the pISce-Dest backbone using Gateway cloning (Fig. 1A) (Kwan et al., 2007). F0 animals

[1]Northeastern University, Department of Biology, Boston, MA 02115, USA. [2]University of Massachusetts Boston, Department of Biology, Boston, MA 02125, USA. [3]University of Kentucky, Department of Biology, Lexington, KY 40506, USA.

*Author for correspondence (j.monaghan@northeastern.edu)

T.J.D., 0000-0002-4945-0294; A.W.S., 0000-0001-6576-3664; C.D.M., 0000-0003-0127-433X; J.R.M., 0000-0002-6689-6108

Handling Editor: Ken Poss
Received 31 March 2021; Accepted 18 February 2022

Development (2022) 149, dev199637. doi:10.1242/dev.199637

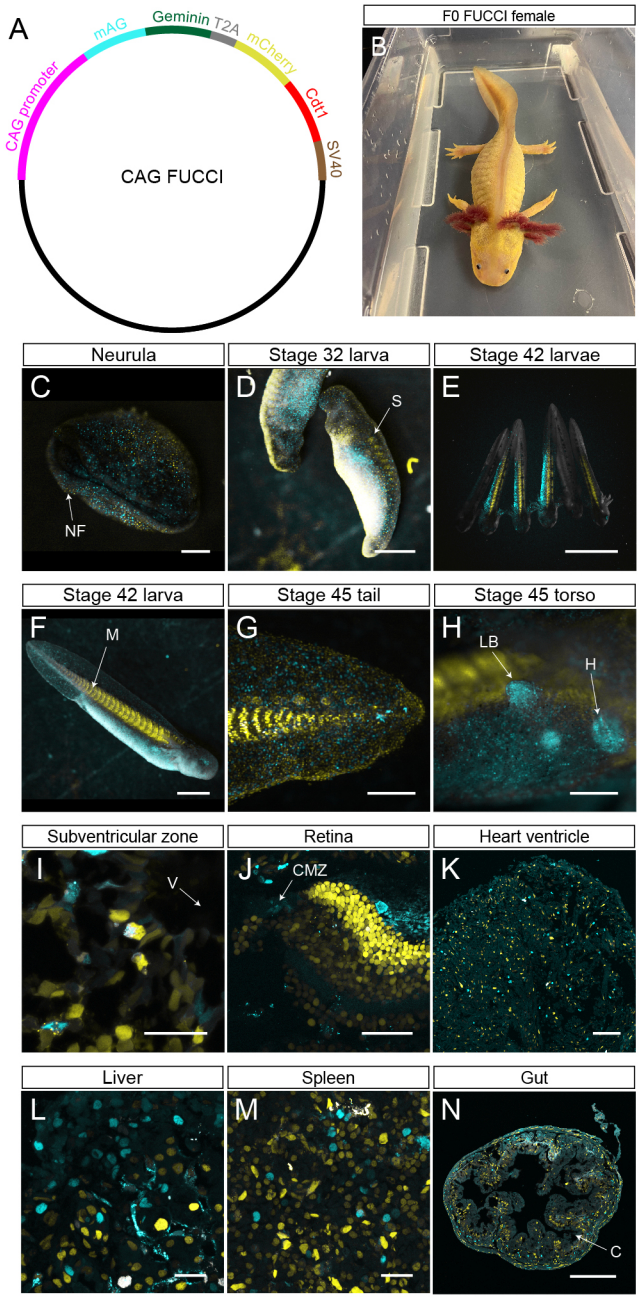

Fig. 1. FUCCI probes are expressed in developing and adult homeostatic tissue. (A) Plasmid map for the CAG-FUCCI construct. (B) A sexually mature, F0 FUCCI female that was crossed with white d/d males to generate the F1 clutch used in the study. (C) Stage 17 neurula expressing FUCCI probes. NF, neural fold. Scale bar: 500 µm. (D) Stage 32 larva. S, somite. Scale bar: 1 mm. (E) Six stage 42 larvae with negative, ubiquitous and variable expression patterns. Scale bar: 5 mm. (F) Individual stage 42 larva. M, myomeres. Scale bar: 1 mm. (G) Posterior tail tip of a stage 45 larva. Scale bar: 500 µm. (H) Torso of a stage 45 larva. LB, limb bud; H, heart. Scale bar: 500 µm. (I) Subventricular zone of the adult brain. V, ventricle. Scale bar: 50 µm. (J) Adult retina. CMZ, ciliary marginal zone. Scale bar: 100 µm. (K) Adult heart ventricle. Scale bar: 100 µm. (L) Adult liver. Scale bar: 50 µm. (M) Adult spleen. Scale bar: 50 µm. (N) Adult gut. C, crypt. Scale bar: 200 µm. Individual channels for I-N are available with EdU staining in Fig. S1. Organs from I-N were harvested from 10-12 cm animals aged 9 months.

were generated using standard axolotl injection conditions with I-SceI Meganuclease (Khattak et al., 2009), generating F0 animals with mosaic FUCCI expression. A single female was selected due to strong ubiquitous FUCCI expression (Fig. 1B) to mate with a d/d white male, which generated clutches consisting of 82% and 92.7% transmission rates, suggesting the FUCCI construct integrated multiple times in the founder animal. To confirm this, we crossed F1 FUCCI animals to a F1 FUCCI sibling or a d/d white animal. In each cross, we observed a non-mendelian distribution of offspring (Table S1), confirming the presence of multiple integrations in the F1 generation. F2 larvae exhibit similar mAG and mCherry expression patterns to the F1 generation throughout embryonic development (data not shown). All subsequent experiments in the following sections were conducted on FUCCI animals from the F1 generation.

Examining live transgenic embryos, we first detected FUCCI protein expression at neurulation with increasing expression throughout development (Fig. 1C,D). Expression was variable between siblings, possibly due to varying levels of transcriptional activation or the presence of multiple integrations of the FUCCI construct into the genome (Fig. 1D-F). Gross observation of transgenic larvae clearly showed distinct non-proliferative G1 populations, including the somites (Fig. 1D), the tail myotomes (Fig. 1G), lateral line neuromasts (Fig. 1G) and highly proliferative S/G2/M populations, such as the limb bud and larval heart (Fig. 1H). To determine the adult expression pattern of F1 FUCCI offspring, tissues sections were analyzed from the brain, eye, heart, liver, spleen and gut. mAG and mCherry expression were observed in every tissue type with little overlap between probes except for differentiated muscle fibers (Fig. 1I-N, Fig. S1).

FUCCI probes overlap with S- and M-phase markers, and correlate with DNA content

To determine the overall expression level of the FUCCI construct in F1 animals, we quantified 2547 cells from FUCCI spinal cords pulsed with ethynyldeoxyuridine (EdU) for 3 h (n=9). In total, 22.34% of the cells were $mAG^+/mCherry^-$, 71.22% were $mAG^-/mCherry^+$, 2.75% were $mAG^+/mCherry^+$ and 3.69% $mAG^-/mCherry^-$ (Fig. S2A). Interestingly, we observed few $mAG^+/mCherry^+$ cells. This observation is corroborated in similar FUCCI axolotl lines (Costa et al., 2021), and is likely because the cells are in a regenerative environment where they are receiving mitogens instructing them to enter the cell cycle instead of resting at the G1/S boundary (Takahashi et al., 2021). We next determined whether mAG^+ cells were specific to the S phase by performing click-it based EdU detection of DNA synthesis on the same regenerating spinal cord tissues. Fig. 2A illustrates the expected pattern of labeling for mAG, mCherry, EdU and phosphorylated serine 10 histone H3 (pHH3). Of the 532 EdU^+ cells (20.9% of total cells), 88.93% were $mAG^+/mCherry^-$, 3.00% were $mAG^+/mCherry^+$, 1.88% were $mAG^-/mCherry^+$ and 6.19% were $mAG^-/mCherry^-$ (Fig. 2B, Fig. S2D). Conversely, 76.68% of mAG^+ cells were EdU^+ and 23.32% of mAG^+ cells were EdU^- (Fig. S2B,D), suggesting that the majority of mAG^+ cells were in S phase rather than G2/M phases. This suggests that the S phase is longer than the combined G2/M phases by approximately threefold, which is supported by previous studies (McCullough and Tassava, 1976). To study mitosis in a highly proliferative tissue, we performed immunohistochemistry with pHH3 in 10 dpa regenerating limb blastemas (n=3) (Fig. S2E-H‴). We found that 88.89% of $pHH3^+$ cells were $mAG^+/mCherry^-$, 4.44% were $mAG^+/mCherry^+$, 0% were $mAG^-/mCherry^+$ and 6.67% were $mAG^-/mCherry^-$ (Fig. 2C). Furthermore, we found that 3.91% of mAG^+ cells were $pHH3^+$ whereas 96.09% were $pHH3^-$ (Fig. S2C), suggesting that the vast majority of mAG^+ limb blastema cells are in S/G2 phases.

Development (2022) 149, dev199637. doi:10.1242/dev.199637

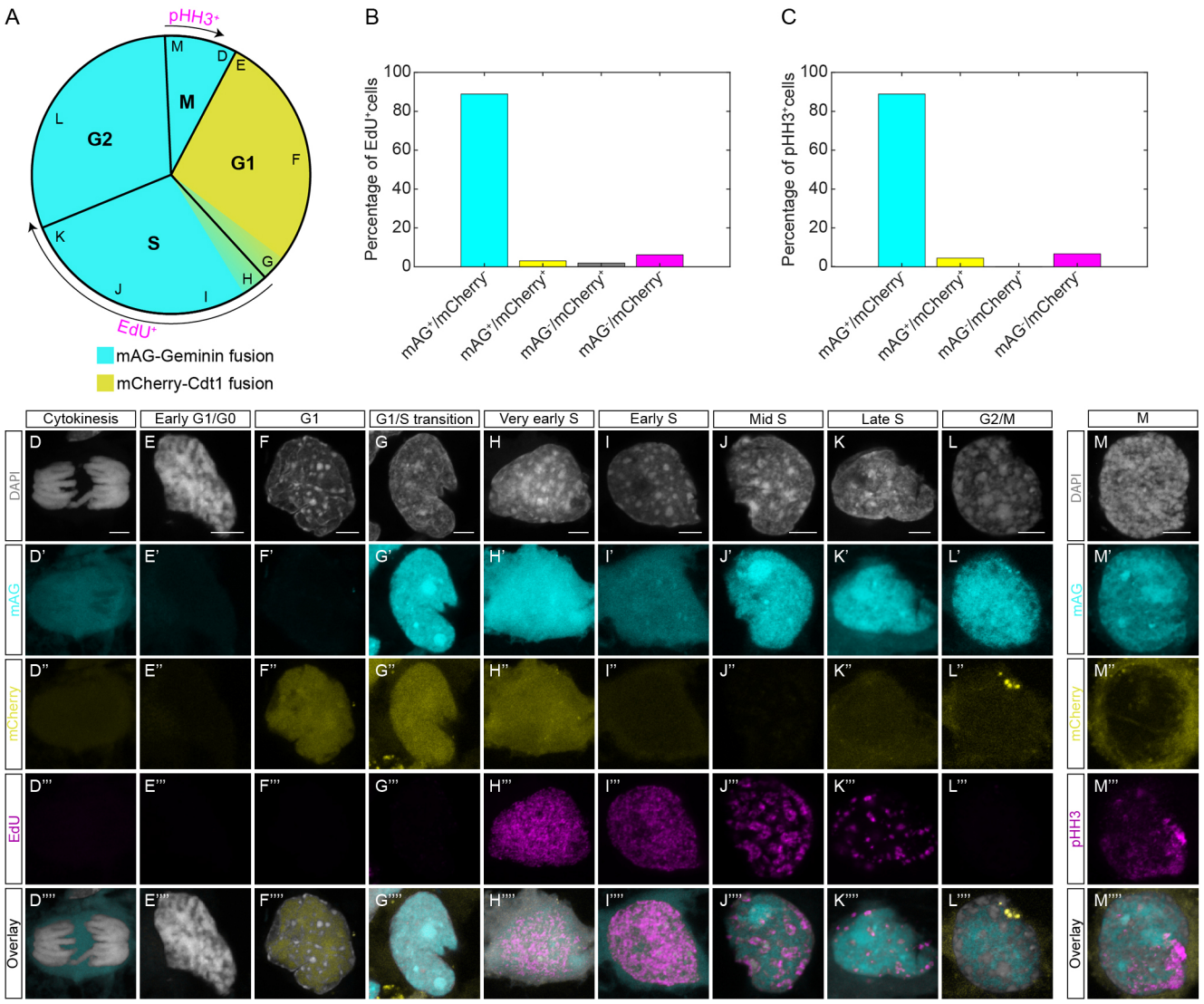

Fig. 2. Validation of FUCCI expression with EdU and pHH3. (A) Schematic of the cell cycle with expected staining patterns of EdU and pHH3. EdU may label cells in early G2 as a result of a 3 h chase and pHH3 weakens during late M phase. Letters at the outer edge of the schematic represent the stage in the cell cycle of cells from D-M. (B) Characterization of EdU$^+$ cells in 14 dpa regenerating spinal cords (n=9). (C) Characterization of pHH3$^+$ cells in 10 dpa regenerating limb blastemas (n=3). (D-L‴) Individual cells from EdU-pulsed spinal cords at every cell cycle stage. Scale bars: 5 µm. (M-M‴) Individual cell in M stage from a limb blastema stained for pHH3. Scale bar: 5 µm. Tissue from B-M‴ was harvested from 8-10 cm animals aged 6 months.

As expected, some pHH3$^+$ had neither probe signal, as Geminin is known to degrade in the late stages of M phase (McGarry and Kirschner, 1998). Overall, the high correspondence between EdU and pHH3 with mAG expression shows that mAG-zGem effectively marks cells in both S and M phases.

We next identified cells at each stage of the cell cycle according to DAPI and EdU staining. Each stage of the cell cycle was observed in proliferating tissues and had predictable genomic structure, EdU incorporation (Leonhardt et al., 2000), pHH3 staining and FUCCI reporter expression (Fig. 2D-M). Importantly, we observe mAG$^+$/mCherry$^+$/EdU$^+$ cells (Fig. 2H), indicating the presence of cells in very early S phase. These cells have not yet fully degraded mCherry but have started translating mAG while incorporating EdU in early S phase. These cells have not yet fully degraded mCherry-zCdt1 but have switched from degrading mAG-zGem to mCherry-zCdt1. Collectively, these results demonstrate that our FUCCI construct correctly and reproducibly labels specific stages of the cell cycle.

To correlate DNA content with FUCCI probes, we dissociated FUCCI limb blastemas and stained the single-cell suspension with Hoechst DNA stain. These cells were then analyzed with FACS based on FUCCI probe fluorescence and Hoechst intensity (Fig. S3A-B″). Imaging both unsorted and sorted cells within the mAG$^+$/mCherry$^-$, mAG$^-$/mCherry$^+$ and mAG$^+$/mCherry$^+$ gates showed pure populations of the respective fluorescent signal (Fig. S3C-F‴). We found that 84% of the mAG$^-$/mCherry$^-$ population was within the 2N gate, while 65.8% of the mAG$^+$/mCherry$^+$ population was within the 4N gate, validating the 2N and 4N gates (Fig. S3B″). We found that 69% of the mAG$^-$/mCherry$^+$ (G1) population was within the 2N gate, and 30.1% was within the 4N gate (Fig. S3B″). These percentages shifted in the mAG$^+$/mCherry$^-$ (S/G2/M) population, where we observed that 59.5% and 40.2% of cells fell within the 2N and 4N gates, respectively (Fig. S3B″). Although the shift in DNA content fits the expected trend for each population, we had expected there to be a larger percentage of both the G1

Development (2022) 149, dev199637. doi:10.1242/dev.199637

population within the 2N gate and the S/G2/M population to be within the 4N gate. We suspect this is due to heterogeneity within the blastema population for two reasons. First, bright-field images of the pre-sorted single celled suspension reveal cells of different sizes and granularity, all with varying degrees of mCherry and mAG fluorescence (Fig. S3C-C‴). Second, the histogram of Hoechst staining in the entire blastema population does not have two well-defined 2N and 4N peaks (Fig. S3B). Together, these data indicate that the different cells within the blastema mesenchyme may vary in their Hoechst fluorescent signal in both the 2N and 4N states. Future studies evaluating the FUCCI signal within specific cell types that contribute to the blastema may resolve this heterogeneity issue.

In vivo imaging of FUCCI expression

To determine the feasibility of *in vivo* imaging of FUCCI tissue, we imaged cycling epithelial cells on the surface of an anesthetized stage 32 larva mounted in 0.3% agarose (Movie 1). Fig. 3A-E depicts a single magnified mAG^+ cell from Movie 1 completing the process of mitosis in under 30 min to produce two daughter cells with fading mAG intensity (Fig. 3A-E, Movie 2). During this process, we observe the formation of the mitotic spindle in prophase and cytokinesis after chromosome separation. We did not observe any cell transition from $mAG^+/mCherry^-$ to $mAG^-/mCherry^+$, or vice versa. This is likely due to the shortening of the G1 phase during embryonic development (Siefert et al., 2015), which would prevent the accumulation of mCherry protein to provide a detectable

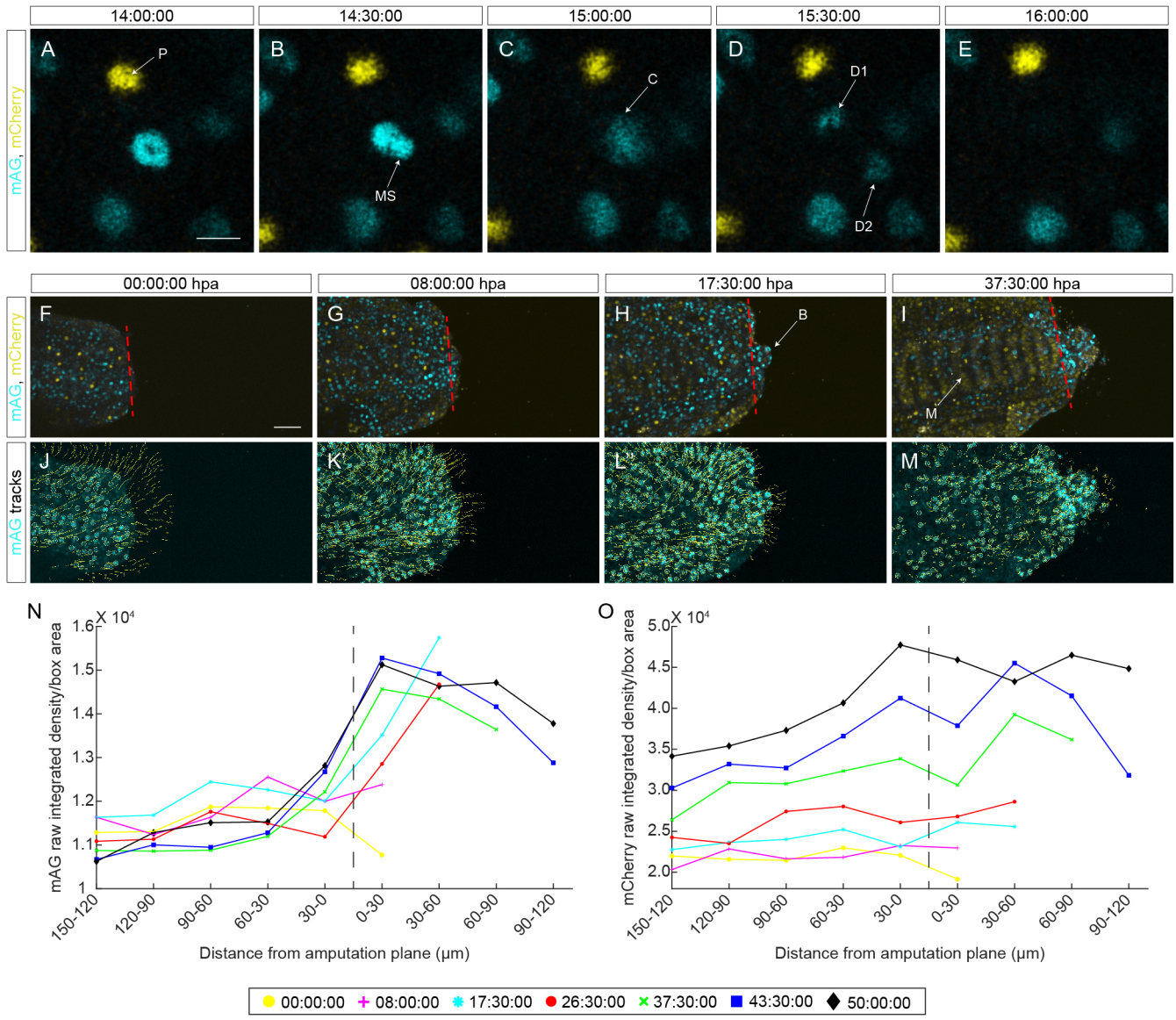

Fig. 3. Continuous live imaging of FUCCI tissue. (A-E) A 2-h time-lapse shown in five 30-min intervals of a dividing epithelial cell from a stage 32 larva. P, pigment cell; MS, mitotic spindle; C, cytokinesis; D1, daughter cell 1; D2, daughter cell 2. Scale bar: 25 µm. (F-I) Four frames from the 60 h live image that depict a regenerating tail ~30 min after amputation (F), after wound healing (G), during blastema formation (H) and during blastema growth (I). The red vertical dashed line represents the amputation plane. B, blastema; M, myomeres. Scale bar: 50 µm. (J-M) Tracks depicting cell migration in F-I. Each line represents the path a cell took 20 frames before the current frame and 20 frames after. (N,O) Charts depicting mAG raw integrated density/area (N) or mCherry raw integrated density/area (O) for seven frames from the 60 h live image. Measurements were obtained by dividing the AP axis of the regenerating tail into boxes with a width of 30 µm (Fig. S4). The vertical dashed line represents the amputation plane.

Development (2022) 149, dev199637. doi:10.1242/dev.199637

signal while transitioning from M phase or before transitioning to S phase.

To visualize blastema formation *in vivo*, we performed live imaging of a regenerating tail in a stage 36 FUCCI animal (Fig. 3F-I). After amputation, the anesthetized larva was immediately embedded in 0.3% agarose and imaged every 30 min over 60 h (Movie 3). During this 60 h imaging experiment, we observed early wound healing (Fig. 3G), blastema formation (Fig. 3H) and myomeric muscle development (Fig. 3I). By 8 h post-amputation (hpa), the tail stump was completely covered by a thin layer of both mAG^+ cells and $mCherry^+$ cells (Fig. 3G). Shortly afterwards, an early blastema was observed in the posterior tail tip by 17.5 hpa (Fig. 3H) that mostly comprised mAG^+ cells. At this time point, early myomeric muscle formation was observed along the anteroposterior (AP) axis of the tail, characterized by regularly spaced bar-shaped groups of $mCherry^+$ cells (Fig. 3H,I). By 37.5 hpa, mAG^+ cells at the amputation plane started accumulating at the base of the blastema (Fig. 3I). After ∼40 h of imaging, cells in the blastema seemed to be dying. However, subsequent time points showed continued maturation of the tail myomere muscle and a general shift from mostly mAG^+ cells in the tail to $mCherry^+$ cells.

To track migrating and dividing mAG^+ cells in the regenerating tail, we used TrackMate (Tinevez et al., 2017). With this, we tracked the position of mAG^+ cells 10 h before and after each frame (Fig. 3J-M, Movie 4). This allowed us to visualize the path cells took to contribute to the regenerated tail. Interestingly, during the early blastema formation phase, we observed a general trend for dorsal tail cells to migrate dorsally, ventral cells to migrate ventrally, and cells in the midline to migrate in the direction of the blastema (Fig. 3J,K). At later time points in the movie, we observed that the intense mAG^+ cells adjacent to the amputation plane were migrating into the tail blastema (Fig. 3M).

We quantified changes in fluorescence of mAG by dividing the regenerating tail into rectangles with a 30 µm width anterior and posterior to the amputation plane (Fig. S4). The raw integrated density for each channel was measured for each box and normalized to the total tail area within each rectangle, providing a measure of intensity per area. These results showed an increase in the intensity of mAG fluorescence in rectangles starting 30 µm anterior to the amputation plane and continuing into the regenerating tail tip, indicating that proliferation is highest in the blastema and in cells 30 µm anterior to the amputation plane (Fig. 3N). Anterior to the amputation plane, the mAG intensity was higher at the earliest time points and steadily decreased after 60 h of imaging (Fig. 3N). The opposite trend was observed for mCherry fluorescence, where the intensity increased after 60 h of imaging (Fig. 3O). These results indicate an increase in the total number of cells in G1 phase, which may represent an accumulation of cells in the resting state after rapid proliferation during early embryonic development.

Multimodal imaging provides cell type identity to FUCCI tissues

The use of two fluorescent proteins in FUCCI sensors limits the acquisition of cell type information, precluding robust cell characterization using imaging modalities including immunohistochemistry (IHC) and fluorescence *in situ* hybridization (FISH) in conjunction with FUCCI probes. To overcome this limitation, we observed that mAG and mCherry can be sufficiently photobleached after imaging to allow for multimodal imaging (Fig. 4A). We first performed version 3 hybridization chain reaction FISH (V3.HCR-FISH) (Choi et al., 2018) for *Shh* using Alexa-fluor 647 on an EdU pulsed, homeostatic FUCCI spinal cord (Fig. 4B, Fig. S5A-A‴). We next photobleached the endogenous FUCCI signal and removed the *Shh* probes with 80% formamide (Fig. 4C, Fig. S5B-B‴). Then a subsequent round of V3.HCR-FISH was performed for *Pax7* and *B3Tub* (Fig. 4D, Fig. S5C-C‴). Imaging and subsequent removal of these probes were followed by EdU labeling (Fig. 4E, Fig. S5D-D‴). EdU signal was then removed with DNase, and IHC was performed for B3TUB (Fig. 4F, Fig. S5E-E‴). The images from each round were aligned to the DAPI image from the first round, allowing imaging of four modalities (transgenic reporter, FISH, click-chemistry and IHC) in the same tissue section (Fig. 4G-J). This analysis shows that cell type identification can be performed along with the study of cell division in FUCCI tissue.

Regenerating FUCCI limbs reveal distinct regions of proliferative and non-proliferative zones in the limb blastema

To visualize cell cycling following limb amputation, we imaged uninjured limbs (Fig. 5A,A′) and regenerating limbs from five animals at 1, 3, 5, 7, 10, and 14 dpa (Fig. 5B-G′). To quantify the location of proliferation following amputation, we calculated the average distance between the amputation plane and the distal $mCherry^+$ muscle boundary line. We found that mAG^+ cells were abundant proximal to the amputation plane as early as 1 dpa, and that these mAG^+ cells were located on average 243.85 µm proximal to the amputation plane (Fig. S6A). This distance from the amputation plane was significantly larger than the same measurement at 5, 7, and 14 dpa (one-way ANOVA with a Tukey-Kramer multiple comparisons, $P<0.05$). These findings correspond well with previous studies, where it was determined that cells located up to 500 µm proximal to the amputation plane participate in regeneration (Currie et al., 2016). As the limb regenerates, we observed fewer mAG^+ cells proximal to the amputation as more mAG^+ cells accumulated within the blastema (Fig. S6A). This observation suggests that the supply of proliferating cells becomes less dependent on cells proximal to the amputation plane at later time points during regeneration.

To determine the cell type of the mAG^+ and $mCherry^+$ cells in regenerating limbs, we visualized FUCCI probe expression in whole-mount with light-sheet fluorescence microscopy (Fig. 5H-N, Fig. S6B-J, Movies 5 and 6). Based on cell morphology, we observed that the majority of uninjured tissue, including fibroblasts, epithelial cells and chondrocytes were $mCherry^+$. Most muscle cells observed were $mAG^+/mCherry^+$, which is consistent with a similar G1/S arrest in FUCCI mouse cardiomyocytes (Alvarez et al., 2019). Very few mAG^+ cells were observed in uninjured tissue (Fig. S6C, Movie 5). At 1 dpa, we observed several mAG^+ cell types, including the wound epithelium, perichondrium and some fibroblasts of the mesenchyme (Fig. S6D). These cell types appear to remain mAG^+ until blastema formation at 7 dpa, where fewer chondrocytes, perichondrial cells and epithelial cells are mAG^+ (Fig. S6E-G). From 7 to 14 dpa, most of the mAG^+ cells are located within the mesenchyme, further showing that cells proximal to the amputation plane less frequently proliferate at later time points during limb regeneration (Fig. S6H,I). By 21 dpa, most of the mAG^+ cells are chondrocytes in the regenerating carpals and digits (Fig. S6B,J, Movie 6). At 10 and 14 dpa, we observed a small population of cells at the distal-most tip of the blastema that were $mAG^-/mCherry^+$ (Fig. 5F′-G′). We sectioned EdU-pulsed 10 dpa blastemas for histological analysis ($n=3$) and found that this $mAG^-/mCherry^+$ population comprised the distal-most epithelial cells of the AEC (Fig. S7A-B‴). In one sample, a small number of these cells was observed in the distal-most region of the blastema mesenchyme

Development (2022) 149, dev199637. doi:10.1242/dev.199637

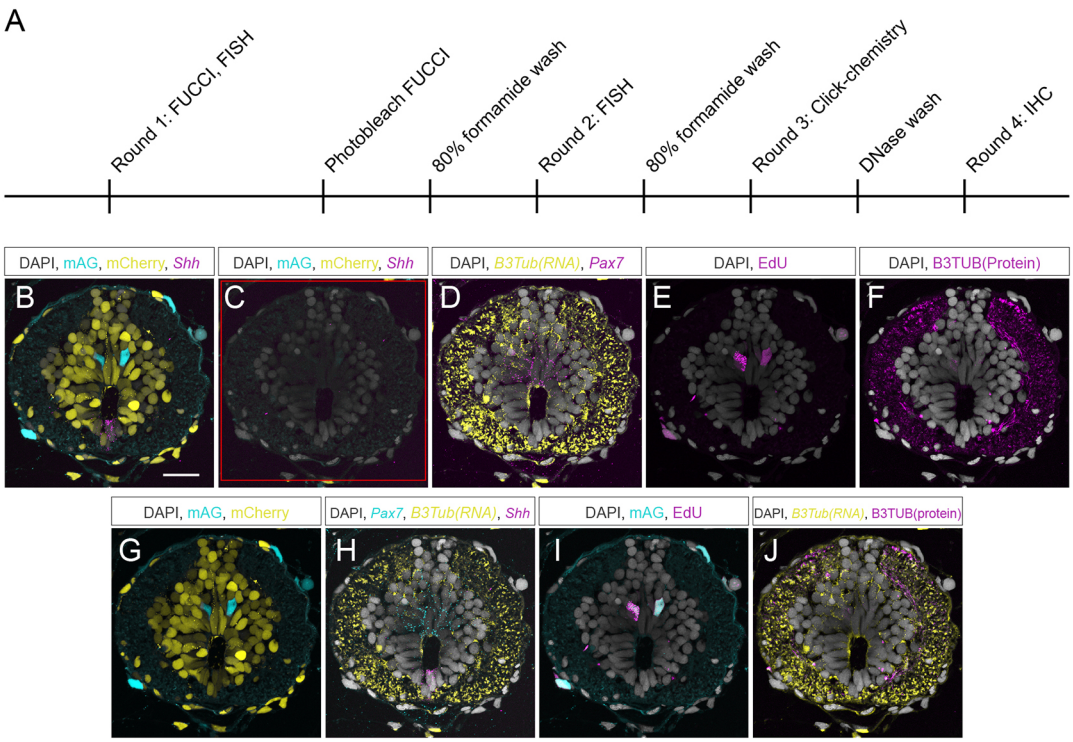

Fig. 4. Multimodal imaging of FUCCI tissue for cell-type characterization and identification of cycling cells. (A) Schematic of the staining timeline used for multimodal imaging in a homeostatic spinal cord. (B) Round one of imaging for endogenous FUCCI signal and *Shh* RNA with V3.HCR-FISH. Scale bar: 50 µm. (C) Round one of imaging after photobleaching. The red square in the panel represents the area photobleached. (D) Round two of imaging for *Pax7* and *B3Tub* RNA with V3.HCR-FISH. The intense signal in the white matter is autofluorescence. (E) Round three of imaging for EdU labeled cells with click-chemistry. (F) Round four of imaging for B3TUB protein with IHC. (G) Endogenous FUCCI signal in the spinal cord. (H) *Pax7*, *B3Tub* RNA and *Shh* V3.HCR-FISH signal from rounds one and two. (I) mAG expression and EdU labeling from rounds one and three. (J) *B3Tub* RNA and B3TUB protein from rounds two and four. DAPI image used for B-J was obtained in round one. Tissue was harvested ∼1 cm from the end of the tail from an 8 cm animal aged 6 months.

(Fig. S7A). We then sectioned 14 dpa blastemas (n=3) and observed the presence of these distal-most, mesenchymal mAG^{-}/mCherry^{+} cells in all three samples (Fig. S7C-E‴), suggesting that this population of cells is more abundant at later stages of regeneration. The observation that the highest proliferation levels are located in the middle-proximodistal region of the blastema has been observed by others in salamanders (Farkas et al., 2016; McCusker et al., 2015b) and in regenerating zebrafish fins (Hirose et al., 2014).

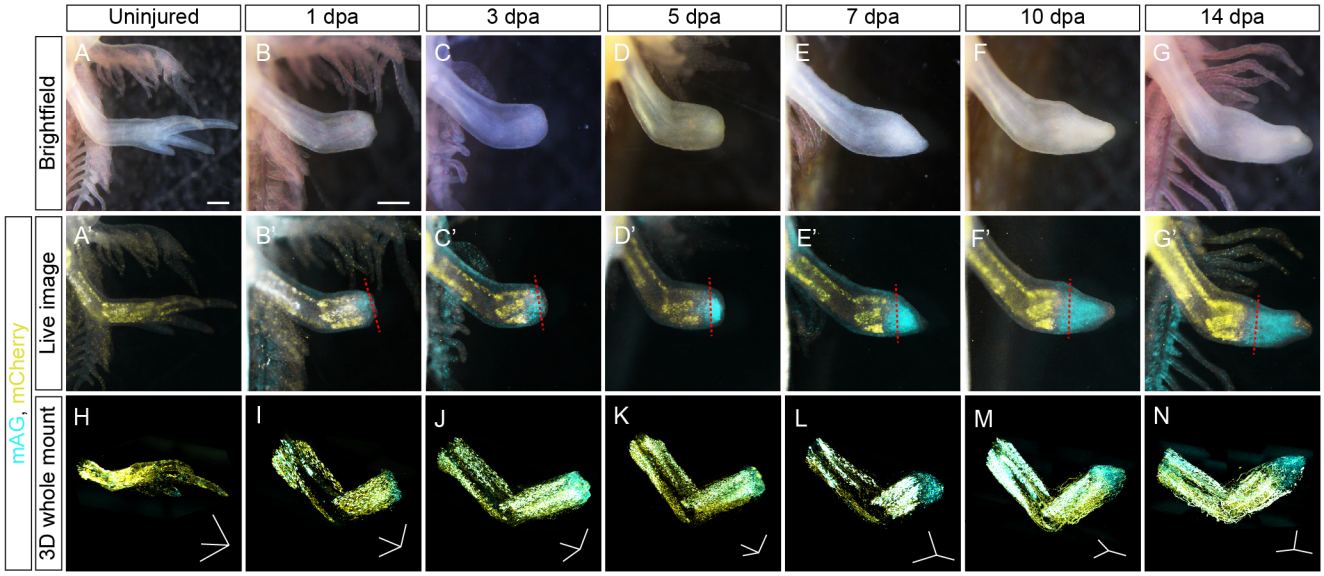

Fig. 5. FUCCI visualization and quantification during limb regeneration. (A-G) Bright-field images of uninjured (A) and regenerating FUCCI limb amputated through the wrist at 1, 3, 5, 7, 10 and 14 dpa (B-G) (n=5 2 cm animals aged 2 months). Scale bars: 500 µm. (A′-G′) mAG and mCherry fluorescence of limbs from A-G. (H-N) 3D whole-mount images of FUCCI limbs obtained by light-sheet fluorescence microscopy. Scale bars: 600 µm in each axis.

Development (2022) 149, dev199637. doi:10.1242/dev.199637

For quantification of blastema cells, we performed flow cytometry analysis on 10 dpa FUCCI blastemas (n=10) (Fig. S8A-D). In total, 5682 cells were analyzed from the total 10,000 events. Of these cells, 25.2% mAG$^+$/mCherry$^-$, 53.9% were mAG$^-$/mCherry$^+$, 1.1% were mAG$^+$/mCherry$^+$ and 16.3% were mAG$^-$/mCherry$^-$. Although these results do not exactly correspond with our tissue section quantification (n=3), where we found that 44.68% were mAG$^+$/mCherry$^-$, 14.96% were mAG$^-$/mCherry$^+$, 14.06% were mAG$^+$/mCherry$^+$ and 26.3% were mAG$^-$/mCherry$^-$, it is not surprising considering that some mCherry$^+$ muscle cells immediately proximal to the blastema were collected for dissociation (Fig. S8E). Additionally, the amount of autofluorescent blood, as well as the cessation of proliferation that likely occurs as the cells are dissociated before FACS analysis, may contribute to the discrepancy.

Blastema cells arrest in G1 phase in the absence of an intact nerve supply

Transection of the nerve supply to the limb inhibits limb regeneration (Farkas and Monaghan, 2017; Todd, 1823). In the absence of nerves, cell proliferation, DNA synthesis rates and the relative number of mitoses in regenerating limbs are all lower than in innervated limbs (Duerr et al., 2020; Kumar et al., 2007; Loyd and Tassava, 1980; Mescher and Tassava, 1975; Monaghan et al., 2009; Tassava et al., 1974). However, our knowledge of how nerves regulate the cell cycle is incomplete. To better understand the impact of denervation on cell cycle regulation in the blastema, we performed FACS analysis on innervated and denervated FUCCI blastemas (Fig. 6). Forelimbs were bilaterally amputated and, at 17 dpa (early/mid bud stage), right limbs were denervated at the brachial plexus while left limbs remained innervated (n=11 blastemas per condition). To ensure enough time for a cellular response to denervation, blastema cells were dissociated 48 h after denervation (Fig. 6A-B‴) and the number of mAG$^+$/mCherry$^-$, mAG$^-$/mCherry$^+$, mAG$^+$/mCherry$^+$ and mAG$^-$/mCherry$^-$ cells from innervated and denervated blastemas (wound epithelium removed) were quantified with FACS (Fig. 6C,D). Our data indicate that denervation decreases the number of mAG$^+$/mCherry$^-$ blastema cells from 17% in innervated to 15% in denervated, with an increase in the number of mAG$^-$/mCherry$^+$ cells from 64% in innervated to 66.2% in denervated (Fig. 6E,F). Furthermore, the number of mAG$^+$/mCherry$^+$ cells decreases from 16.5% in innervated limbs to 14.7% in denervated, and the number of mAG$^-$/mCherry$^-$ cells increases from 2.4% in innervated to 4.2% in denervated (Fig. 6E,F). Together, these results indicate that, in the absence of nerves, some blastema cells arrest in G1 phase (decrease

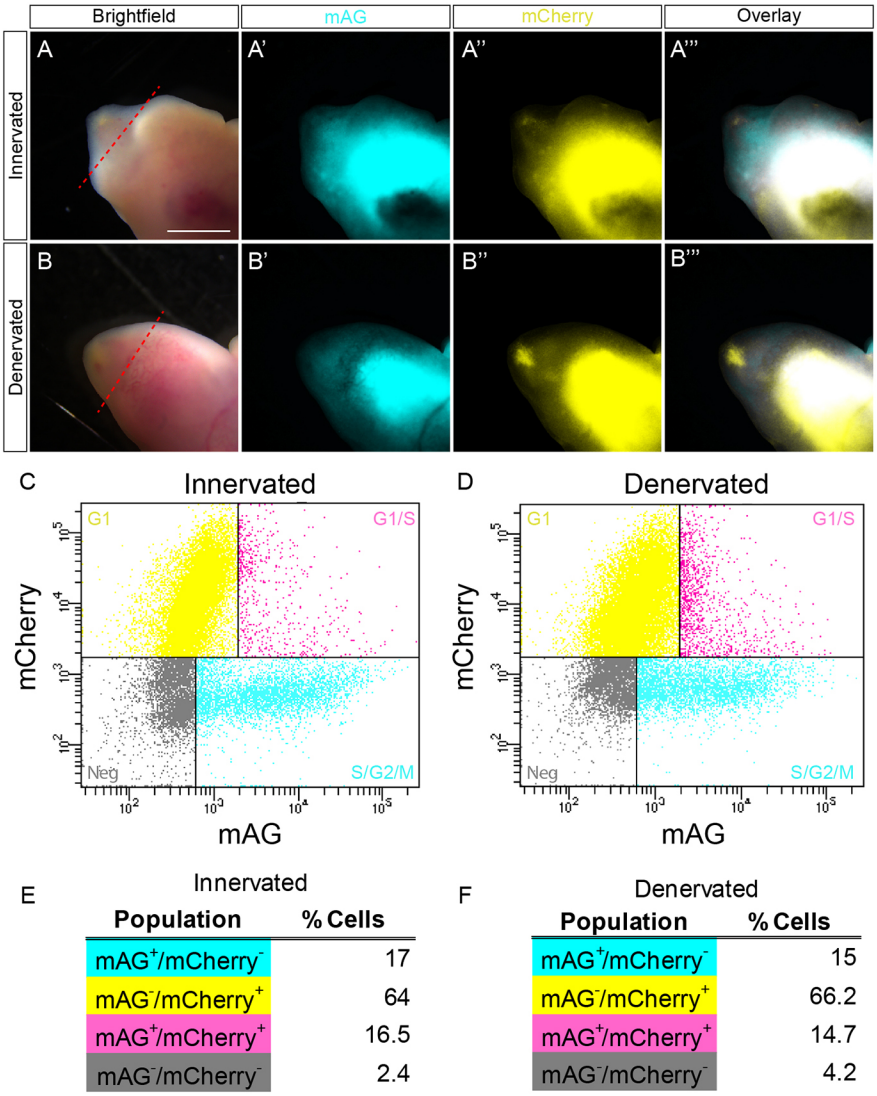

E

Innervated

Population	% Cells
mAG$^+$/mCherry$^-$	17
mAG$^-$/mCherry$^+$	64
mAG$^+$/mCherry$^+$	16.5
mAG$^-$/mCherry$^-$	2.4

F

Denervated

Population	% Cells
mAG$^+$/mCherry$^-$	15
mAG$^-$/mCherry$^+$	66.2
mAG$^+$/mCherry$^+$	14.7
mAG$^-$/mCherry$^-$	4.2

Fig. 6. Limb denervation arrests blastema cells in G1 phase. (A-B‴) Individual channels for innervated limbs (A-A‴) and limbs denervated 48 h earlier (B-B‴). Scale bar: 2.0 mm. (C,D) Scatter plots of mAG versus mCherry fluorescent blastema cells from innervated (C) and denervated (D) FUCCI limbs (n=11, 15-18 cm animals aged 1 year). Gates were established as described in the Materials and Methods. (E,F) Tables depicting the percentage of blastema cells within each gate out of the total number of blastema cells.

Development (2022) 149, dev199637. doi:10.1242/dev.199637

in the number of $mAG^+/mCherry^-$ and $mAG^+/mCherry^+$ cells, increase in the number of $mAG^-/mCherry^+$ cells) or exit the cell cycle (increase in the number of $mAG^-/mCherry^-$ cells).

Spinal cord amputation induces a proliferation response 5 mm from the injury

To determine the location of proliferating cells along the AP axis of the regenerating spinal cord, we collected 14 dpa EdU pulsed FUCCI spinal cords (n=4) and obtained tissue sections at various locations along the AP axis in relation to the most posterior tip of the regenerated cartilaginous rod (Fig. 7A, Table S2). The amputation plane is located between the 250 µm anterior and 500 µm anterior sections, as the notochord was identified 500 µm anterior to the cartilaginous rod but not at the 250 µm anterior section. For comparison, we sectioned spinal cords from non-regenerating, homeostatic FUCCI animals (n=5) (Table S2). Quantification included cells within the boundary of the meninges that surrounds the spinal cord but excluded the meningeal cells themselves (Fig. 7B). $mAG^+/mCherry^-$ cells were consistently around 40% of total cells posteriorly and progressively declined anteriorly (Fig. 7C-L), which may indicate that cell proliferation is most abundant at or posterior to the cartilaginous rod tip. This is accompanied by an increase in the number of $mAG^-/mCherry^+$ cells anteriorly along the regenerating AP axis (Fig. 7C-L), suggesting a shortened G1 phase in regenerating cells that is supported by previous studies (Rodrigo Albors et al., 2015). Furthermore, we observed a significant increase in the number of $mAG^+/mCherry^-$ cells located 5000 µm from the regenerated cartilaginous rod compared with uninjured spinal cords (two-tailed Student's t-test assuming unequal variances, P=0.0043), suggesting that spinal cord injury induces an increase in cell cycling beyond 500 µm anterior to the amputation plane (Fig. 7L, Table S2). Our results also indicate that the relative abundance of cells in S or G2/M, as indicated by mAG^+/EdU^+ or mAG^+/EdU^-, respectively, is unchanged across the AP axis (Fig. 7M, Table S2), suggesting that the ratio of S:G2 does not significantly change across the regenerating AP axis. However, a significant difference is detected between the total number of mAG^+/EdU^+ cells detected in sections 5000 µm from the cartilaginous rod tip and uninjured spinal cords (two-tailed Student's t-test assuming unequal variances, P=0.001) (Fig. 7M). A statistically significant difference between the number of mAG^+/EdU^- cells at these regions was not detected (two-tailed Student's t-test assuming unequal variances, P=0.143) (Fig. 7M). Taken together, our results indicate that spinal cord injury induces an increase in the number of cycling cells along the AP axis nearly 5 mm from the injury compared with uninjured controls.

DISCUSSION

The use of FUCCI sensors in the axolotl enables the study of cell cycle dynamics during tissue regeneration that were previously hindered without an *in vivo* marker of cell state. By using the FUCCI system, we validated findings from previous studies, including the mostly local recruitment of cells required for limb (Butler, 1933) and tail regeneration (McHedlishvili et al., 2007). We also uncovered new findings regarding the impact of the nerve on the cell cycle during limb regeneration, showing that blastema cells arrest in G1 phase after severing the nerve supply. This could be explained by the absence of mitogenic factors supplied by the nerve, such as NRG1 (Farkas et al., 2016), transferrin (Mescher and Munaim, 1984) and FGFs/BMPs (Makanae et al., 2014). We also show the presence of proliferative ependymal cells in the spinal cord almost 5 mm from the site of injury. Several explanations exist for the proliferative response in the spinal cord, including a systemic proliferation response after injury (Johnson et al., 2018), an organ-wide proliferation response as seen in the regenerating lung (Jensen et al., 2021) or proliferation induced by neuronal death (Hedlund et al., 2016). These results demonstrate the power of FUCCI sensors for the study of cell cycle dynamics during tissue regeneration. Recently, others have developed a similar FUCCI system in the axolotl to explore cell cycle dynamics in the regenerating spinal cord (Costa et al., 2021). These FUCCI animal lines will provide an important tool to the community to better understand how the cell cycle is regulated in the axolotl during tissue regeneration. This knowledge is crucial for informing regenerative medicine to induce a more-robust proliferative response in mammals after spinal cord injury or limb amputation.

Many fundamental questions remain unanswered regarding cell proliferation during appendage regeneration. How cell cycle dynamics change during regeneration compared with uninjured limbs, whether the cell cycle length is unique to individual regenerating organs, and whether the cell cycle is regulated differently during development versus regeneration are among some of the many unresolved issues. Previously, these questions were addressed using a combination of thymidine analogs such as EdU and BrdU, pHH3 antibody labeling, and mitotic figures. However, none of these methods provides information about multiple cell cycle stages and they are unable to be used for live imaging. FUCCI axolotls provide a powerful means with which to address these questions in detail while improving the existing toolbox for the study of cell cycle dynamics during tissue regeneration. Furthermore, a major advantage of using FUCCI sensors in the axolotl is the amenability of axolotl embryonic tissue to grafting, which can be used to label limb connective tissue, muscle cells, epithelium, Schwann cells, vasculature, neural stem cells, neural crest cells and teeth primordium (Epperlein et al., 2012; Kragl et al., 2009; Kragl and Tanaka, 2009; Nacu et al., 2013). Grafting FUCCI tissue onto white embryos will allow tissue-specific expression without the need for the generation of new transgenic animals with a tissue-specific promoter driving FUCCI expression.

Although FUCCI sensors in the axolotl are highly useful, some limitations exist. One issue of our transgenic line is the variable expression across animals and tissues. This is particularly obvious in adult animals, where some animals seem to strongly express only one fluorescent protein. Continuous breeding of the line to d/d mates should decrease variability across siblings. The use of EdU in FUCCI tissue also has small limitations. First, the number of $mAG^+/mCherry^-/EdU^-$ cells may be underrepresented and the number of $mAG^+/mCherry^-/EdU^+$ may be overrepresented; after a 3 h pulse of EdU, cells labeled in late S phase will transition to G2 phase before collection. The severity of this issue can be reduced by collecting tissue sooner than 3 h after the EdU pulse, but this problem is theoretically always possible. Second, we observed the presence of $mAG^-/mCherry^+/EdU^+$ and $mAG^-/mCherry^-/EdU^+$ cell populations in our samples. Our quantification suggests that these populations are not highly abundant, and we speculate that they are detected as a result of the cells not expressing the FUCCI construct or DNA damage, as EdU is known to be incorporated into cells undergoing DNA repair (Verbruggen et al., 2014). An interesting finding in our study is the abundance of mAG^-/EdU^+ enterocytes in the axolotl gut (Fig. S1F-F‴). One explanation for this could be the rapid clonal expansion and migration of enterocytes from the intestinal crypt to the tip of the villi. This is supported by a decrease in EdU intensity at the tip of the villi, suggesting EdU dilution after division despite a relatively short 3 h pulse of EdU. More studies on the cell cycle length in the intestinal

Development (2022) 149, dev199637. doi:10.1242/dev.199637

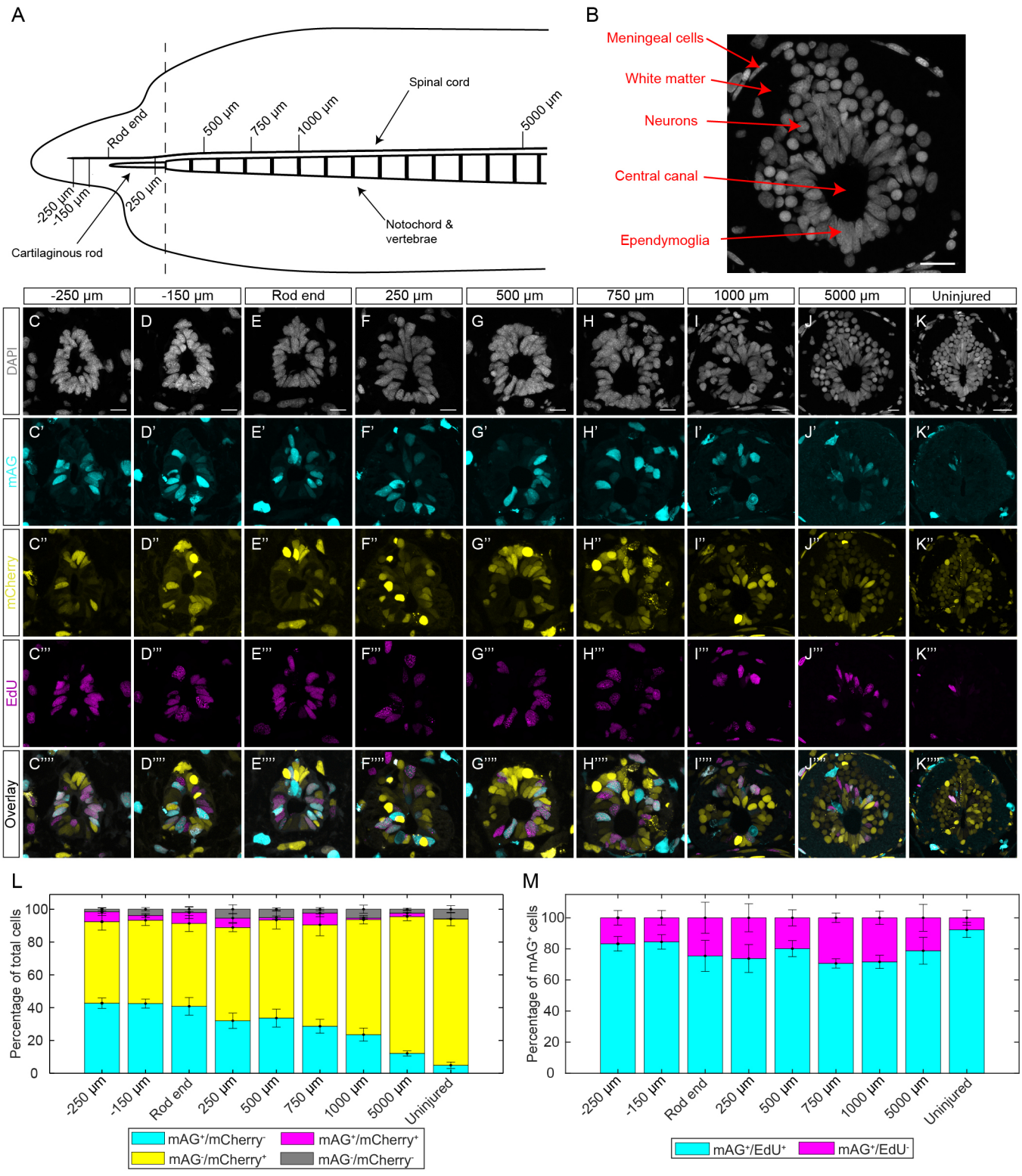

Fig. 7. Spinal cord amputation induces a proliferative response 5 mm from the amputation plane at 14 dpa. (A) Schematic of the experiment. (B) Cell types of the spinal cord. Scale bar: 25 µm. (C-K‴) Individual channels for spinal cord cross-sections pulsed with EdU (*n*=4 for regenerating spinal cords, *n*=5 for uninjured spinal cords, 8-10 cm animals aged 6 months). Scale bars: 25 µm for C-J‴; 50 µm for K-K‴. (L) Total cell quantification across the regenerating AP axis. (M) mAG$^+$ cell characterization across the regenerating AP axis. Data are mean±s.e.m.

stem cell niche in the axolotl are required to elucidate this phenomenon.

In our study, we highlight the versatility of imaging FUCCI tissue with live imaging, whole-mount imaging and multimodal imaging. To our knowledge, we present the first real time movie of blastema formation in regenerating axolotl tail. The approaches used in this study will be helpful for other groups attempting to capture live images of appendage regeneration in real-time, but methods should

Development (2022) 149, dev199637. doi:10.1242/dev.199637

be optimized. During blastema growth, we observed a large number of dying cells and cells sluffing from the blastema. After removing the larvae from the agarose, we also noticed that the blastema was misshapen. We suspect that this is not a true representation of tail blastema growth and is more likely a result of the blastema growing in the agarose. However, we cannot exclude the possibility of live cell extrusion (Chen et al., 2016; Eisenhoffer et al., 2012) or apoptosis. Using available programs for cell tracking, we also demonstrate the capability for tracking FUCCI cells during the regenerative process. Although images were taken every 30 min, we cannot be absolutely certain about the fate of some cells given this time interval without identification of specific cells. We also visualized FUCCI expression in whole-mount regenerating limbs with light-sheet fluorescence microscopy. We attempted to visualize these limbs in 3D after staining for EdU, but the EdU signal from the 647 channel bled into the mCherry signal. With better filtering, we expect to be able to perform 3D multiscale analysis of DNA synthesis in FUCCI tissue (Duerr et al., 2020).

Finally, we outline a method for cell characterization in transgenic tissue with multimodal imaging. These proof of concept experiments demonstrate that robust cell type information can be acquired from FUCCI tissue sections despite the endogenous mAG and mCherry signal. We foresee better cell type characterization via multimodal imaging with more rounds of FISH, multiple macromolecule analogs with unique click-it compatible functional groups (Duerr et al., 2020), and multiple primary antibodies raised in different species. One potential limitation of this method is the inefficiency of photobleaching FUCCI signal in large tissues. The spinal cord is an ideal organ for this analysis, as it can easily fit into a single 20X frame. Thus, photobleaching is contained to one single tile. If using larger tissue like a limb blastema, many more tiles may require photobleaching and at potentially a lower magnification, both of which will increase the time necessary to completely photobleach the FUCCI signal. Nevertheless, our method can be used for the robust characterization of cycling cells during tissue regeneration. We expect that these methods can also be applied in other transgenic reporter axolotl lines and other animal models.

MATERIALS AND METHODS

Animal procedures

All transgenic animals were bred at Northeastern University, and all procedures and surgeries were approved by the Northeastern University Institutional Animal Care and Use Committee. Surgeries were performed while axolotls were anesthetized in 0.01% benzocaine. EdU was administered via intraperitoneal injection at 8.0 ng/g animal and samples were collected 3 h after injection.

Transgenesis

Transgenesis was performed via I-SceI meganuclease digestion according to Khattak et al. (2009). Briefly, 1 µg of purified, CAG-FUCCI plasmid (Addgene #175266) was mixed in solution with 1 µl NEB Cutsmart buffer and 1 µl I-SceI enzyme, filled to a final volume of 10 µl with nuclease-free water to generate the FUCCI injection cocktail. Single-cell, d/d axolotl embryos were injected with 5 nl of FUCCI injection cocktail and grown to stage 45 for phenotype assessment. Owing to the β-actin promoter in CAG, the most intense FUCCI expression was observed in myomeric muscle of developing tails. Larvae with strong, ubiquitous expression were identified and grown to sexual maturity.

Histology and staining

Samples were fixed in 4% PFA overnight at 4°C, and after washing with 1×PBS three times for 5 min, samples were cryoprotected in 30% sucrose until equilibrated. Samples were then placed in OCT and frozen at −80°C. Frozen samples were sectioned with a cryostat to obtain 10 µm sections. Slides were then baked at 65°C for 15 min. Residual OCT was removed from slides by placing in water for 5 min at room temperature. From this step, the slides are ready for click-chemistry, IHC or FISH.

EdU labeling via click chemistry

For EdU detection, we used an Alexa-fluor 647 azide plus probe from clickchemistrytools.com (product number: 1482). The 1 ml click-it cocktail was made as follows: 888 µl 1×Tris, 10 µl 50 mM $CuSO_4$ (0.5 mM final), 2 µl Alexa-fluor 647 azide plus (2 µM final) and 100 µl 100 mM sodium ascorbate (10 mM final). This cocktail was applied to slides for 30 min at room temperature.

IHC

Slides were incubated in blocking buffer (15 µl goat serum in 1 ml 1× PBS) for 30 min. Rabbit anti-pHH3 antibodies (Cell Signaling, 9701) were diluted in blocking buffer at 1:400 and applied to slides overnight at 4°C. Slides were washed three times for 5 min each with 1× PBS, and Alexa-fluor 647 anti-rabbit secondary antibodies (Invitrogen, A21245; 1:500 in 1× PBS) were applied to slides for 30 min at room temperature.

Multi-round V3.HCR-FISH

All of the following steps were conducted using RNase-free reagents. Slides were placed in 100% ethanol at room temperature for 1 h. Following three 5-min washes with 1× PBS, slides were prehybridized with hybridization buffer (Molecular Instruments) for 30 min at 37°C. Probe stocks for a particular transcript of interest were made to contain 1 µM of each oligo in 200 µl of RNase-free water. Probe sequences for *Shh*, *B3Tub* and *Pax7* are provided in Table S3. Probe stocks were further diluted at 1:200 in hybridization buffer and applied to slides overnight at 37°C. Slides were washed with formamide wash buffer (Molecular Instruments) three times for 15 min at 37°C to remove unbound probe, then washed twice with 5× SSCT (20× saline sodium citrate with 0.1% Tween 20) for 15 min at room temperature. Amplification buffer (Molecular Instruments) was then applied to the slides for 30 min at room temperature. Fluorescent hairpins for each initiator (Molecular Instruments) were prepared by heating H1 and H2 hairpins to 95°C for 90 s. Hairpins were allowed to cool to room temperature in the dark, then diluted 1:50 in amplification buffer and applied to slides overnight at room temperature. Slides were then washed twice for 30 min with 5× SSCT at room temperature.

After these protocols, cell nuclei were stained with DAPI (2.86 µM) for 5 min at room temperature. Following a 5-min 1× PBS wash at room temperature, slides were mounted with SlowFade gold antifade mountant (Thermo S36936) and imaged using a Zeiss LSM 800 confocal microscope.

Live FUCCI imaging

Larvae used for live imaging were mounted in a 50×9 mm Petri dish in 0.3% low melt agarose diluted in 0.005% benzocaine. All live images were acquired using a Zeiss LSM 880 confocal microscope fitted with a humidification chamber to prevent sample desiccation. Larvae were imaged at 10× magnification. For live imaging of tail regeneration, we imaged two adjacent tiles to accommodate for growth during imaging at 10× magnification. Additionally, to accommodate cells moving in and out of the focal plane, we imaged four planes in the *z*-axis spanning 119.4 µm and merged these planes in a maximum intensity projection. To prevent photobleaching of the FUCCI probes, we used 1.0% laser power for each channel. Larvae were removed from agarose after imaging and placed in salamander housing water. Larvae were swimming and feeding 1 week after imaging with no visible signs of illness or distress.

Multimodal imaging

EdU-pulsed FUCCI spinal cords were collected as outlined above. In the first round of multimodal imaging, we performed V3.HCR-FISH for *Shh* with 647 hairpins. The endogenous FUCCI signal and V3.HCR-FISH was then imaged. To photobleach the FUCCI signal, the 488 and 594 lasers were set to 100% laser power and were directed onto the spinal cord for 40 min. We found that the DAPI signal was weakened after this photobleaching, but was still present. The V3.HCR-FISH signal was sufficiently photobleached,

but to ensure *Shh* probes were not amplified in the subsequent round of FISH, the slides were washed with 80% formamide four times for 15 min each at 37°C. The slides were washed in 5× SSCT twice for 15 min each at room temperature, prehybridized with hybridization buffer for 30 min at 37°C, and rehybridized with *Pax7* and *B3Tub* probes for the second round of multimodal imaging. These probes were amplified with 647 and 488 hairpins, respectively. Slides were imaged, and probes were again removed with four 15 min washes of 80% formamide at 37°C. Slides were washed three times with 1× PBS, and the click-it cocktail outlined above was used with Alexa-fluor 647 azide plus probes for EdU labeling in the third round of multimodal imaging. Slides were imaged and treated with DNase I (NEB M0303) overnight at room temperature. DNase I was applied to slides without buffer, and enough was used to cover the entire section being imaged. The next day, we performed IHC with rabbit anti-B3TUB antibodies (Invitrogen, PA5-85639; 1:500) and applied anti-rabbit Alexa-fluor 647 antibodies the subsequent day. Slides were then imaged for the final round of multimodal imaging. Adobe Photoshop was used to align the images from each round onto the original DAPI image. All images were obtained with a Zeiss LSM 800 confocal microscope.

Whole-mount FUCCI imaging

To prepare whole mount-tissue, limbs were fixed in 4% PFA overnight at 4°C. Limbs were then washed with 1× PBS three times for 5 min, and dehydrated in an increasing methanol series (25% methanol/75% 1× PBS, 50% methanol/50% 1× PBS, 75% methanol/25% 1× PBS, each step for 5 min at room temperature), and stored in 100% methanol at −20°C for up to 6 months before imaging. Once ready to be imaged, the limbs were rehydrated in a decreasing methanol series (75% methanol/25% 1× PBS, 50% methanol/50% 1× PBS, 25% methanol/75% 1× PBS, each step for 5 min at room temperature) and washed once with 1× PBS for 5 min. The samples were washed three times with 1× PBST (PBS and 1% Triton X-100) for 5 min at room temperature. We found that a 90 min 0.5% trypsin treatment at room temperature with rocking improved light penetration of FUCCI samples without appreciable changes in intensity of mAG and mCherry. After trypsin treatment, samples were washed with deionized water three times for 5 min at room temperature. The limbs were then placed in 100% acetone for 20 min at −20°C. Afterwards, the samples were incubated in deionized water for 10 min at room temperature. Samples were again washed with 1× PBS three times for 5 min, mounted in 1.5% low melt agarose and refractive index matched with EasyIndex RI 1.465 (LifeCanvas Technologies) overnight at 4°C. Three-dimensional images were obtained using a Zeiss light-sheet Z1 microscope with Zen software. All post-processing for visualization was performed using Arivis software.

Cell dissociation, Hoechst staining and flow cytometry

Blastemas from the d/d strain or FUCCI animals were collected and pooled together in a six-well plate. The wound epithelium was not surgically removed. Blastemas were incubated on ice in 0.35 mg/ml Liberase for 20 min and were then incubated at room temperature with gentle agitation. Every 10 min, the tissue was manually dissociated with forceps by teasing the tissue apart. This was repeated until there was a sufficient single-cell suspension (checked under the microscope) while the wound epithelium remained intact. The wound epithelium was manually removed with forceps from the suspension. 1 ml of 80% PBS was added to the cell suspension prior to filtering in a 35 µm filter tube. The strainer was then washed with an additional 1 ml of 80% PBS.

The filtered single-cell suspensions were run on a BD FACSAria Fusion Cell Sorter (UMass Boston Flow Cytometry Core) using the 100 µm nozzle and the FSC 2.0 ND filter. The gates for the blastema cell population were set on the blastema cells from a d/d animal using forward and side scatter. Using the forward scatter and side scatter plot, the cell population was gated to separate it from debris and doublets. A sample of the gated population was sorted, and the presence of singlet cells was confirmed with fluorescence microscopy.

To identify the fluorescent negative blastema cells from the FUCCI animals, we first used blastema samples from d/d strain axolotls. To identify the red or green fluorescent populations, we first plotted each fluorescent channel versus forward scatter. Both plots yielded two discrete populations: a mAG^{-}/$mCherry^{-}$population, which overlapped with the previously identified fluorescent negative gate described above; and a fluorescent positive population. The mAG and mCherry fluorescent populations were each gated, and these gates were used to establish quadrant gates in the FITC (mAG) versus PE-Texas Red (mCherry) scatter plot. The quadrant gates were added to quantify the mAG^{-}/$mCherry^{+}$ (G1 phase), mAG^{+}/$mCherry^{-}$ (S, G2 and M phases) and mAG^{+}/$mCherry^{+}$ (G1 to S transition) populations. Gates for fluorescent populations were also confirmed by sorting and validating cell populations with fluorescence microscopy.

To analyze the DNA content in each of the FUCCI populations, samples were stained with Hoechst for DNA content analysis. Hoechst was added to the single-cell suspension at a final concentration of 1.62 µM for 10 min at room temperature before filtering through a cell strainer. The lack of clear separation between the 2N and 4N peaks in the Hoechst channel required the use of the red and green fluorescent-negative population to gate the 2N population in the Hoechst channel. The 4N gate was set around the cell populations with stronger Hoechst staining than the 2N gate. Using these parameters, 84% of the mAG^{-}/$mCherry^{-}$ fluorescent population was in the 2N gate, and 65% of the mAG^{+}/$mCherry^{+}$ cells were in the 4N gate.

Data analysis

$FUCCI^{+}$ cells were quantified either manually in Adobe Photoshop or with Cellpose (Stringer et al., 2021) combined with custom Fiji scripts (Schindelin et al., 2012), which have been deposited in GitHub (https://github.com/Monaghan-Lab/FUCCI-macros). Fiji scripts for quantification of mAG/mCherry intensity changes during tail regeneration have also been deposited in GitHub (https://github.com/Monaghan-Lab/FUCCI-macros). Limb blastema amputation plane to $mCherry^{+}$ muscle line measurements were made using the InteredgeDistance macro on Fiji. Data processing and statistical analysis were conducted in Microsoft Excel and Matlab.

Acknowledgements

The authors thank Jackson Griffiths for assisting with transgenic animal care during the COVID-19 pandemic lockdown, Ester Comellas for assistance with data analysis, both Guoxin Rong and Alex Lovely for imaging assistance, and Malcolm Maden for early conceptual discussions on the project. Images were obtained from the Northeastern University Chemical Imaging of Living Systems core. We thank the Institute for Chemical Imaging of Living Systems at Northeastern University for consultation and imaging support. Non-transgenic animals were obtained from the Ambystoma Genetic Stock Center, which is funded by the National Institutes of Health (P40OD019794).

Competing interests

The authors declare no competing or financial interests.

Author contributions

Conceptualization: T.J.D., A.W.S., J.R.M.; Methodology: T.J.D., A.V., J.R.M.; Software: A.V.; Validation: T.J.D.; Formal analysis: T.J.D., A.V.; Investigation: T.J.D., E.K.J., K.M.W., J.R.M.; Resources: C.D.M., J.R.M.; Data curation: T.J.D.; Writing - original draft: T.J.D., K.M.W., C.D.M., J.R.M.; Writing - review & editing: T.J.D., E.K.J., A.V., A.W.S., C.D.M., J.R.M.; Visualization: T.J.D., E.K.J., A.V.; Supervision: J.R.M.; Project administration: J.R.M.; Funding acquisition: J.R.M.

Funding

The work from this paper was funded by the National Institutes of Health (R01HD099174) and by the National Science Foundation (1558017 and 1656429). Funding for A.V. and E.K.J. was partially provided by the National Science Foundation (REU grant 1757443). Deposited in PMC for release after 12 months.

Peer review history

The peer review history is available online at https://journals.biologists.com/dev/article-lookup/doi/10.1242/dev.199637.

References

Abe, T., Sakaue-Sawano, A., Kiyonari, H., Shioi, G., Inoue, K.-I., Horiuchi, T., Nakao, K., Miyawaki, A., Aizawa, S. and Fujimori, T. (2013). Visualization of cell cycle in mouse embryos with Fucci2 reporter directed by Rosa26 promoter. *Development* **140**, 237-246. doi:10.1242/dev.084111

Alvarez, R., Jr, Wang, B. J., Quijada, P. J., Avitabile, D., Ho, T., Shaitrit, M., Chavarria, M., Firouzi, F., Ebeid, D., Monsanto, M. M. et al. (2019).

Cardiomyocyte cell cycle dynamics and proliferation revealed through cardiac-specific transgenesis of fluorescent ubiquitinated cell cycle indicator (FUCCI). *J. Mol. Cell. Cardiol.* **127**, 154-164. doi:10.1016/j.yjmcc.2018.12.007

Bouldin, C. M. and Kimelman, D. (2014). Dual fucci: a new transgenic line for studying the cell cycle from embryos to adults. *Zebrafish* **11**, 182-183. doi:10.1089/zeb.2014.0986

Butler, E. G. (1933). The effects of X-radiation on the regeneration of the fore limb of Amblystoma larvae. *J. Exp. Zool.* **65**, 271-315. doi:10.1002/jez.1400650302

Chen, C.-H., Puliafito, A., Cox, B. D., Primo, L., Fang, Y., Di Talia, S. and Poss, K. D. (2016). Multicolor cell barcoding technology for long-term surveillance of epithelial regeneration in Zebrafish. *Dev. Cell* **36**, 668-680. doi:10.1016/j.devcel.2016.02.017

Choi, H. M. T., Schwarzkopf, M., Fornace, M. E., Acharya, A., Artavanis, G., Stegmaier, J., Cunha, A. and Pierce, N. A. (2018). Third-generation in situ hybridization chain reaction: multiplexed, quantitative, sensitive, versatile, robust. *Development* **145**, dev165753. doi:10.1242/dev.165753

Costa, E. C., Otsuki, L., Rodrigo Albors, A., Tanaka, E. M. and Chara, O. (2021). Spatiotemporal control of cell cycle acceleration during axolotl spinal cord regeneration. *eLife* **10**, e55665. doi:10.7554/eLife.55665

Currie, J. D., Kawaguchi, A., Traspas, R. M., Schuez, M., Chara, O. and Tanaka, E. M. (2016). Live imaging of axolotl digit regeneration reveals spatiotemporal choreography of diverse connective tissue progenitor pools. *Dev. Cell* **39**, 411-423. doi:10.1016/j.devcel.2016.10.013

Duerr, T. J., Comellas, E., Jeon, E. K., Farkas, J. E., Joetzjer, M., Garnier, J., Shefelbine, S. J. and Monaghan, J. R. (2020). 3D visualization of macromolecule synthesis. *eLife* **9**, e60354. doi:10.7554/eLife.60354

Eisenhoffer, G. T., Loftus, P. D., Yoshigi, M., Otsuna, H., Chien, C.-B., Morcos, P. A. and Rosenblatt, J. (2012). Crowding induces live cell extrusion to maintain homeostatic cell numbers in epithelia. *Nature* **484**, 546-549. doi:10.1038/nature10999

Epperlein, H.-H., Khattak, S., Knapp, D., Tanaka, E. M. and Malashichev, Y. B. (2012). Neural crest does not contribute to the neck and shoulder in the axolotl (Ambystoma mexicanum). *PLoS ONE* **7**, e52244. doi:10.1371/journal.pone.0052244

Farkas, J. E. and Monaghan, J. R. (2017). A brief history of the study of nerve dependent regeneration. *Neurogenesis (Austin)* **4**, e1302216. doi:10.1080/23262133.2017.1302216

Farkas, J. E., Freitas, P. D., Bryant, D. M., Whited, J. L. and Monaghan, J. R. (2016). Neuregulin-1 signaling is essential for nerve-dependent axolotl limb regeneration. *Development* **143**, 2724-2731. doi:10.1242/dev.133363

Hedlund, E., Belnoue, L., Theofilopoulos, S., Salto, C., Bye, C., Parish, C., Deng, Q., Kadkhodaei, B., Ericson, J., Arenas, E. et al. (2016). Dopamine receptor antagonists enhance proliferation and neurogenesis of midbrain Lmx1a-expressing progenitors. *Sci. Rep.* **6**, 26448. doi:10.1038/srep26448

Hirose, K., Shiomi, T., Hozumi, S. and Kikuchi, Y. (2014). Mechanistic target of rapamycin complex 1 signaling regulates cell proliferation, cell survival, and differentiation in regenerating zebrafish fins. *BMC Dev. Biol.* **14**, 42. doi:10.1186/s12861-014-0042-9

Jensen, T. B., Giunta, P., Schultz, N. G., Griffiths, J. M., Duerr, T. J., Kyerematen, Y., Wong, H., Adesina, A. and Monaghan, J. R. (2021). Lung injury in axolotl salamanders induces an organ-wide proliferation response. *Dev. Dyn.* **250**, 866-879. doi:10.1002/dvdy.315

Johnson, K., Bateman, J., DiTommaso, T., Wong, A. Y. and Whited, J. L. (2018). Systemic cell cycle activation is induced following complex tissue injury in axolotl. *Dev. Biol.* **433**, 461-472. doi:10.1016/j.ydbio.2017.07.010

Khattak, S., Richter, T. and Tanaka, E. M. (2009). Generation of transgenic axolotls (Ambystoma mexicanum). *Cold Spring Harb. Protoc.* **2009**, pdb.prot5264. doi:10.1101/pdb.prot5264

Khattak, S., Schuez, M., Richter, T., Knapp, D., Haigo, S. L., Sandoval-Guzmán, T., Hradlikova, K., Duemmler, A., Kerney, R. and Tanaka, E. M. (2013). Germline transgenic methods for tracking cells and testing gene function during regeneration in the axolotl. *Stem Cell Rep.* **1**, 90-103. doi:10.1016/j.stemcr.2013.03.002

Kragl, M. and Tanaka, E. M. (2009). Grafting axolotl (Ambystoma mexicanum) limb skin and cartilage from GFP+ donors to normal hosts. *Cold Spring Harb. Protoc.* **2009**, pdb.prot5266. doi:10.1101/pdb.prot5266

Kragl, M., Knapp, D., Nacu, E., Khattak, S., Maden, M., Epperlein, H. H. and Tanaka, E. M. (2009). Cells keep a memory of their tissue origin during axolotl limb regeneration. *Nature* **460**, 60-65. doi:10.1038/nature08152

Kumar, A., Godwin, J. W., Gates, P. B., Garza-Garcia, A. A. and Brockes, J. P. (2007). Molecular basis for the nerve dependence of limb regeneration in an adult vertebrate. *Science* **318**, 772-777. doi:10.1126/science.1147710

Kwan, K. M., Fujimoto, E., Grabher, C., Mangum, B. D., Hardy, M. E., Campbell, D. S., Parant, J. M., Yost, H. J., Kanki, J. P. and Chien, C.-B. (2007). The Tol2kit: a multisite gateway-based construction kit for Tol2 transposon transgenesis constructs. *Dev. Dyn.* **236**, 3088-3099. doi:10.1002/dvdy.21343

Leonhardt, H., Rahn, H.-P., Weinzierl, P., Sporbert, A., Cremer, T., Zink, D. and Cardoso, M. C. (2000). Dynamics of DNA replication factories in living cells. *J. Cell Biol.* **149**, 271-280. doi:10.1083/jcb.149.2.271

Loyd, R. M. and Tassava, R. A. (1980). DNA synthesis and mitosis in adult newt limbs following amputation and insertion into the body cavity. *J. Exp. Zool.* **214**, 61-69. doi:10.1002/jez.1402140109

Makanae, A., Mitogawa, K. and Satoh, A. (2014). Co-operative Bmp- and Fgf-signaling inputs convert skin wound healing to limb formation in urodele amphibians. *Dev. Biol.* **396**, 57-66. doi:10.1016/j.ydbio.2014.09.021

McCullough, W. and Tassava, R. (1976). Determination of the blastema cell cycle in regenerating limbs of the larval axolotl, Ambystoma Mexicanum. *Ohio J. Sci.* **76**, 63.

McCusker, C., Bryant, S. V. and Gardiner, D. M. (2015a). The axolotl limb blastema: cellular and molecular mechanisms driving blastema formation and limb regeneration in tetrapods. *Regeneration (Oxf)* **2**, 54-71. doi:10.1002/reg2.32

McCusker, C. D., Athippozhy, A., Diaz-Castillo, C., Fowlkes, C., Gardiner, D. M. and Voss, S. R. (2015b). Positional plasticity in regenerating Amybstoma mexicanum limbs is associated with cell proliferation and pathways of cellular differentiation. *BMC Dev. Biol.* **15**, 45. doi:10.1186/s12861-015-0095-4

McGarry, T. J. and Kirschner, M. W. (1998). Geminin, an inhibitor of DNA replication, is degraded during mitosis. *Cell* **93**, 1043-1053. doi:10.1016/S0092-8674(00)81209-X

McHedlishvili, L., Epperlein, H. H., Telzerow, A. and Tanaka, E. M. (2007). A clonal analysis of neural progenitors during axolotl spinal cord regeneration reveals evidence for both spatially restricted and multipotent progenitors. *Development* **134**, 2083. doi:10.1242/dev.02852

Mescher, A. L. and Munaim, S. I. (1984). "Trophic" effect of transferrin on amphibian limb regeneration blastemas. *J. Exp. Zool.* **230**, 485-490. doi:10.1002/jez.1402300317

Mescher, A. L. and Tassava, R. A. (1975). Denervation effects on DNA replication and mitosis during the initiation of limb regeneration in adult newts. *Dev. Biol.* **44**, 187-197. doi:10.1016/0012-1606(75)90386-3

Monaghan, J. R., Epp, L. G., Putta, S., Page, R. B., Walker, J. A., Beachy, C. K., Zhu, W., Pao, G. M., Verma, I. M., Hunter, T. et al. (2009). Microarray and cDNA sequence analysis of transcription during nerve-dependent limb regeneration. *BMC Biol.* **7**, 1. doi:10.1186/1741-7007-7-1

Nacu, E., Glausch, M., Le, H. Q., Damanik, F. F. R., Schuez, M., Knapp, D., Khattak, S., Richter, T. and Tanaka, E. M. (2013). Connective tissue cells, but not muscle cells, are involved in establishing the proximo-distal outcome of limb regeneration in the axolotl. *Development* **140**, 513. doi:10.1242/dev.081752

Nishitani, H., Lygerou, Z. and Nishimoto, T. (2004). Proteolysis of DNA replication licensing factor Cdt1 in S-phase is performed independently of geminin through its N-terminal region. *J. Biol. Chem.* **279**, 30807-30816. doi:10.1074/jbc.M312644200

Rajan, S. G., Gallik, K. L., Monaghan, J. R., Uribe, R. A., Bronner, M. E. and Saxena, A. (2018). Tracking neural crest cell cycle progression in vivo. *Genesis* **56**, e23214. doi:10.1002/dvg.23214

Rodrigo Albors, A., Tazaki, A., Rost, F., Nowoshilow, S., Chara, O. and Tanaka, E. M. (2015). Planar cell polarity-mediated induction of neural stem cell expansion during axolotl spinal cord regeneration. *eLife* **4**, e10230. doi:10.7554/eLife.10230

Sakaue-Sawano, A., Kurokawa, H., Morimura, T., Hanyu, A., Hama, H., Osawa, H., Kashiwagi, S., Fukami, K., Miyata, T., Miyoshi, H. et al. (2008). Visualizing spatiotemporal dynamics of multicellular cell-cycle progression. *Cell* **132**, 487-498. doi:10.1016/j.cell.2007.12.033

Sandoval-Guzmán, T., Wang, H., Khattak, S., Schuez, M., Roensch, K., Nacu, E., Tazaki, A., Joven, A., Tanaka, E. M. and Simon, A. (2014). Fundamental differences in dedifferentiation and stem cell recruitment during skeletal muscle regeneration in two salamander species. *Cell Stem Cell* **14**, 174-187. doi:10.1016/j.stem.2013.11.007

Schindelin, J., Arganda-Carreras, I., Frise, E., Kaynig, V., Longair, M., Pietzsch, T., Preibisch, S., Rueden, C., Saalfeld, S., Schmid, B. et al. (2012). Fiji: an open-source platform for biological-image analysis. *Nat. Methods* **9**, 676-682. doi:10.1038/nmeth.2019

Siefert, J. C., Clowdus, E. A. and Sansam, C. L. (2015). Cell cycle control in the early embryonic development of aquatic animal species. *Comp. Biochem. Physiol. C Toxicol. Pharmacol.* **178**, 8-15. doi:10.1016/j.cbpc.2015.10.003

Stocum, D. L. (2017). Mechanisms of urodele limb regeneration. *Regeneration* **4**, 159-200. doi:10.1002/reg2.92

Stringer, C., Wang, T., Michaelos, M. and Pachitariu, M. (2021). Cellpose: a generalist algorithm for cellular segmentation. *Nat. Methods* **18**, 100-106. doi:10.1038/s41592-020-01018-x

Sugiyama, M., Sakaue-Sawano, A., Iimura, T., Fukami, K., Kitaguchi, T., Kawakami, K., Okamoto, H., Higashijima, S.-I. and Miyawaki, A. (2009). Illuminating cell-cycle progression in the developing zebrafish embryo. *Proc. Natl. Acad. Sci. USA* **106**, 20812-20817. doi:10.1073/pnas.0906464106

Takahashi, K., Tanabe, R., Ehata, S., Kubota, S. I., Morishita, Y., Ueda, H. R. and Miyazono, K. (2021). Visualization of the cancer cell cycle by tissue-clearing technology using the Fucci reporter system. *Cancer Sci.* **112**, 3796-3809. doi:10.1111/cas.15034

Tanaka, E. M. (2016). The molecular and cellular choreography of appendage regeneration. *Cell* **165**, 1598-1608. doi:10.1016/j.cell.2016.05.038

Tassava, R. A., Bennett, L. L. and Zitnik, G. D. (1974). DNA synthesis without mitosis in amputated denervated forelimbs of larval axolotls. *J. Exp. Zool.* **190**, 111-116. doi:10.1002/jez.1401900110

Tinevez, J. Y., Perry, N., Schindelin, J., Hoopes, G. M., Reynolds, G. D., Laplantine, E., Bednarek, S. Y., Shorte, S. L. and Eliceiri, K. W. (2017). TrackMate: an open and extensible platform for single-particle tracking. *Methods* **115**, 80-90. doi:10.1016/j.ymeth.2016.09.016

Todd, T. J. (1823). On the process of reproduction of the members of the aquatic salamander. *Q. J. Sci. Lit. Arts* **16**, 84-96.

Tsai, S. L., Baselga-Garriga, C. and Melton, D. A. (2020). Midkine is a dual regulator of wound epidermis development and inflammation during the initiation of limb regeneration. *eLife* **9**, e50765. doi:10.7554/eLife.50765

Verbruggen, P., Heinemann, T., Manders, E., von Bornstaedt, G., van Driel, R. and Höfer, T. (2014). Robustness of DNA repair through collective rate control. *PLoS Comput. Biol.* **10**, e1003438. doi:10.1371/journal.pcbi.1003438

Yin, K., Ueda, M., Takagi, H., Kajihara, T., Sugamata Aki, S., Nobusawa, T., Umeda-Hara, C. and Umeda, M. (2014). A dual-color marker system for in vivo visualization of cell cycle progression in Arabidopsis. *Plant J.* **80**, 541-552. doi:10.1111/tpj.12652

Zielke, N. and Edgar, B. A. (2015). FUCCI sensors: powerful new tools for analysis of cell proliferation. *Wiley Interdiscip. Rev. Dev. Biol.* **4**, 469-487. doi:10.1002/wdev.189

Zielke, N., Korzelius, J., van Straaten, M., Bender, K., Schuhknecht, G. F. P., Dutta, D., Xiang, J. and Edgar, B. A. (2014). Fly-FUCCI: a versatile tool for studying cell proliferation in complex tissues. *Cell Rep.* **7**, 588-598. doi:10.1016/j.celrep.2014.03.020

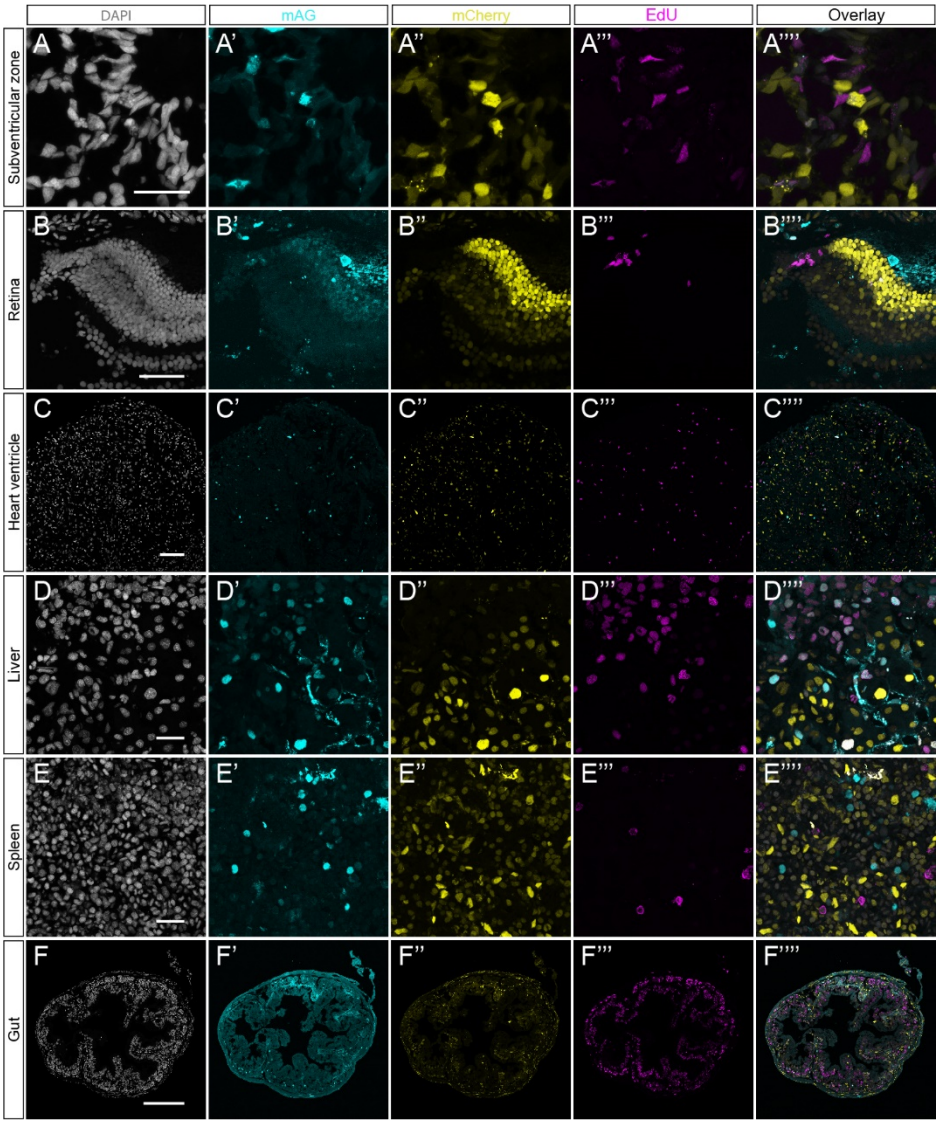

Fig. S1. Single channel images from Figure 1

(A-F'''') Individual channels from panels I-J in Fig. 1 with EdU staining. Scale bars are identical as in Fig. 1.

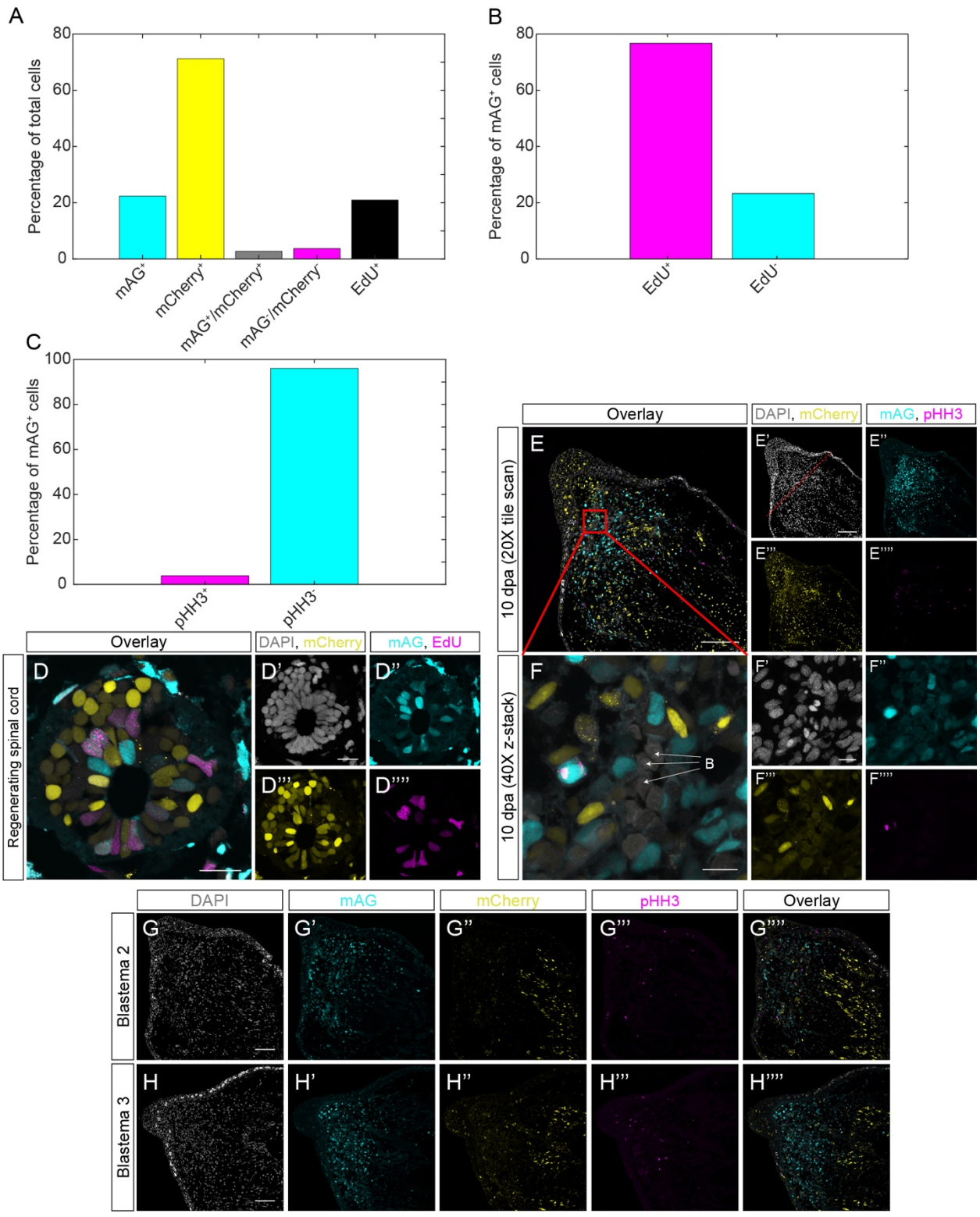

Fig. S2. Additional information from FUCCI validation

(A) Total cell characterization of the 2547 cells from the EdU pulsed 14 dpa regenerating spinal cords. (B) Quantification of the number of mAG^+/EdU^+ and mAG^+/EdU^- cells from the EdU pulsed 14 dpa regenerating spinal cords. (C) Quantification of mAG^+ cells that were $pHH3^+$ or $pHH3^-$ from 10 dpa limb blastemas. (D-D'''') Representative image of an EdU pulsed spinal cord used for quantification in Fig. 2B and Fig. S2B. Scale bars= 25 μm. (E-E'''') 20X tile scan of a 10 dpa FUCCI blastema stained with pHH3. Scale bars= 150 μm. (F-F'''') 40X z-stack of pHH3 stained blastema mesenchyme. B= blood cells. Scale bars= 25 μm. (G-H'''') Two additional replicates of 10 dpa FUCCI limb blastemas stained for pHH3. Scale bars= 100 μm.

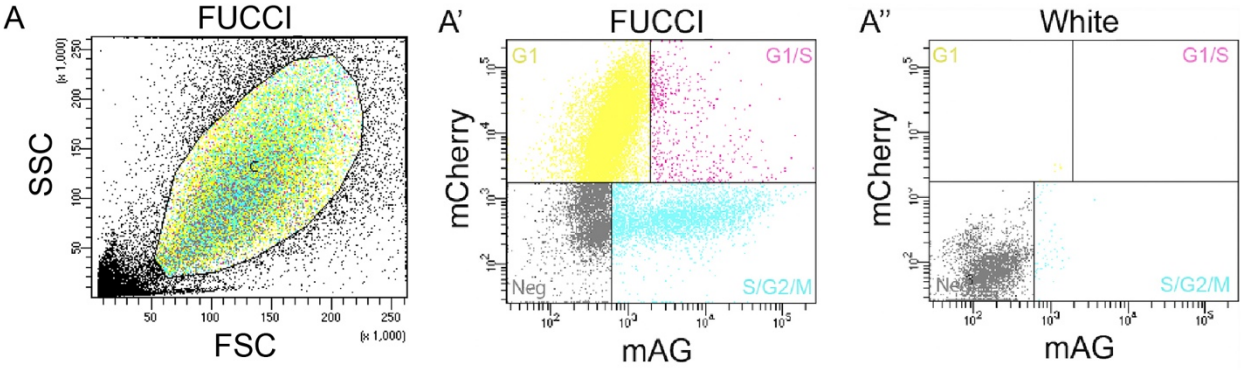

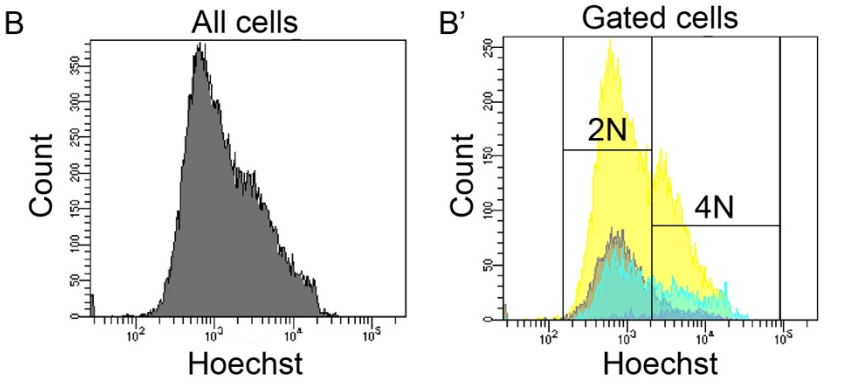

B''

Population	%Parent
mAG⁻/mCherry⁺ *	64
2N**	69
4N**	30.1
mAG⁺/mCherry⁻ *	17
2N**	59.5
4N**	40.2
mAG⁺/mCherry⁺ *	2.4
2N**	33.3
4N**	65.8
mAG⁻/mCherry⁻ *	16.5
2N**	84
4N**	14

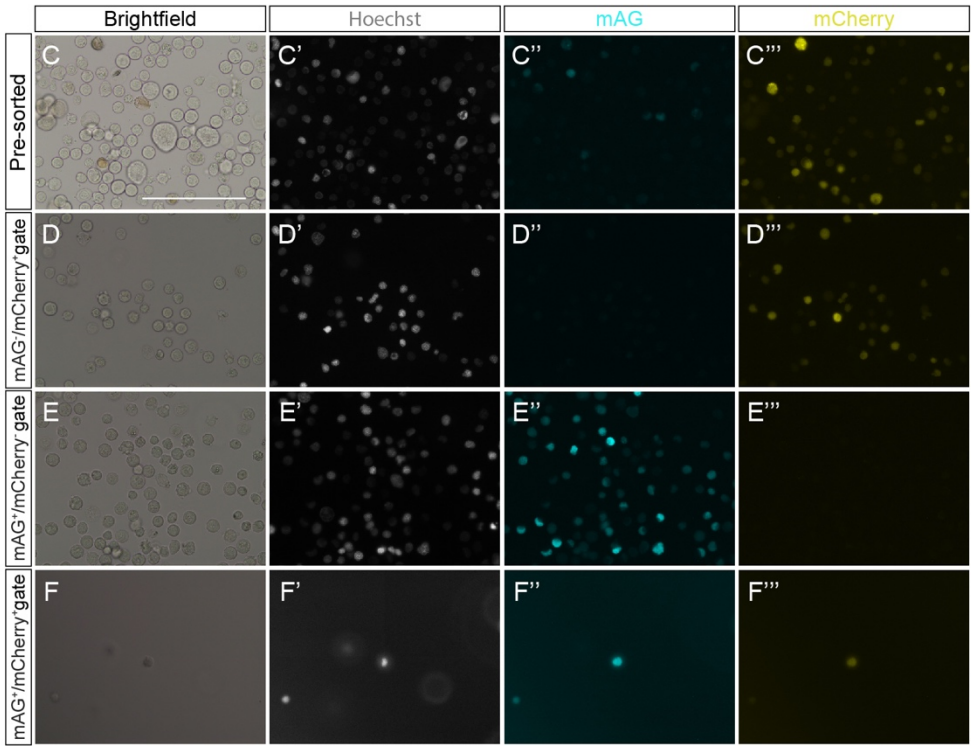

Fig. S3. DNA content correlates with FUCCI probe expression

(A) Scatter plot of FSC vs SSC on a blastema sample from FUCCI animals (n=11, 15-18 cm animals aged 1 year). Data from 10,000 events were collected. The parent gate is set around the blastema singlet population. (A', A") Scatter plots of mAG versus mCherry fluorescence in blastema cells from FUCCI (A') and white strain (A") animals. Quadrant gates delineating the G1 ($mAG^-/mCherry^+$, yellow), S/G2/M ($mAG^+/mCherry^-$, cyan), G1/S ($mAG^+/mCherry^+$, pink), and negative populations ($mAG^-/mCherry^-$, gray) were established as described in the materials and methods. (B-B") Analysis of Hoechst staining on the FUCCI blastema cell population. (B) Histogram of Hoechst stain on all blastema cells. (B') Histogram of Hoechst stain in the G1 ($mAG^-/mCherry^+$), S/G2/M ($mAG^+/mCherry^-$), G1/S ($mAG^+/mCherry^+$), and negative ($mAG^-/mCherry^-$) blastema populations (colors as in A') with the 2N and 4N gates. Gating was performed as described in methods. (B") Table of the percent of 2N and 4N cells from G1 ($mAG^-/mCherry^+$), S/G2/M ($mAG^+/mCherry^-$), G1/S ($mAG^+/mCherry^+$), and negative populations ($mAG^-/mCherry^-$). *= parent population is all cells. **=parent population is the gated population. (C-F'") Sorted cells using the gates established in A'. Scale bar= 200 μm.

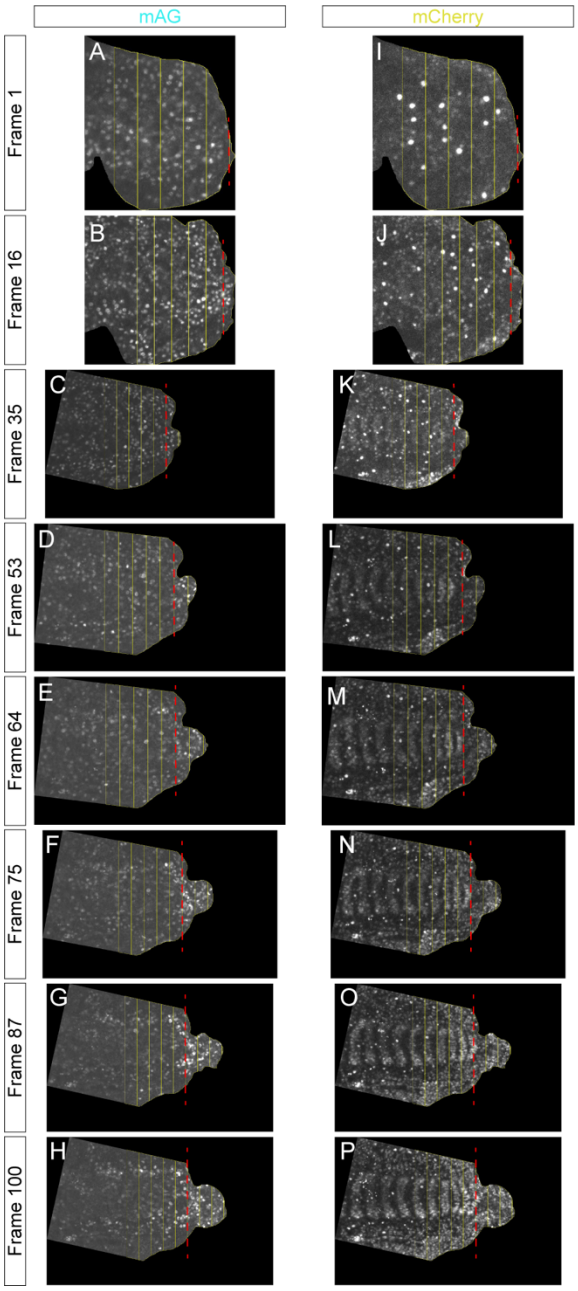

Fig. S4. Tail regeneration live image quantification boxes

(A-H) Frames with quantification boxes for mAG. (I-P) Frames with quantification boxes for mCherry. The red dashed line indicates the amputation plane on each frame. Raw integrated density was measured for each box and divided by the total box area.

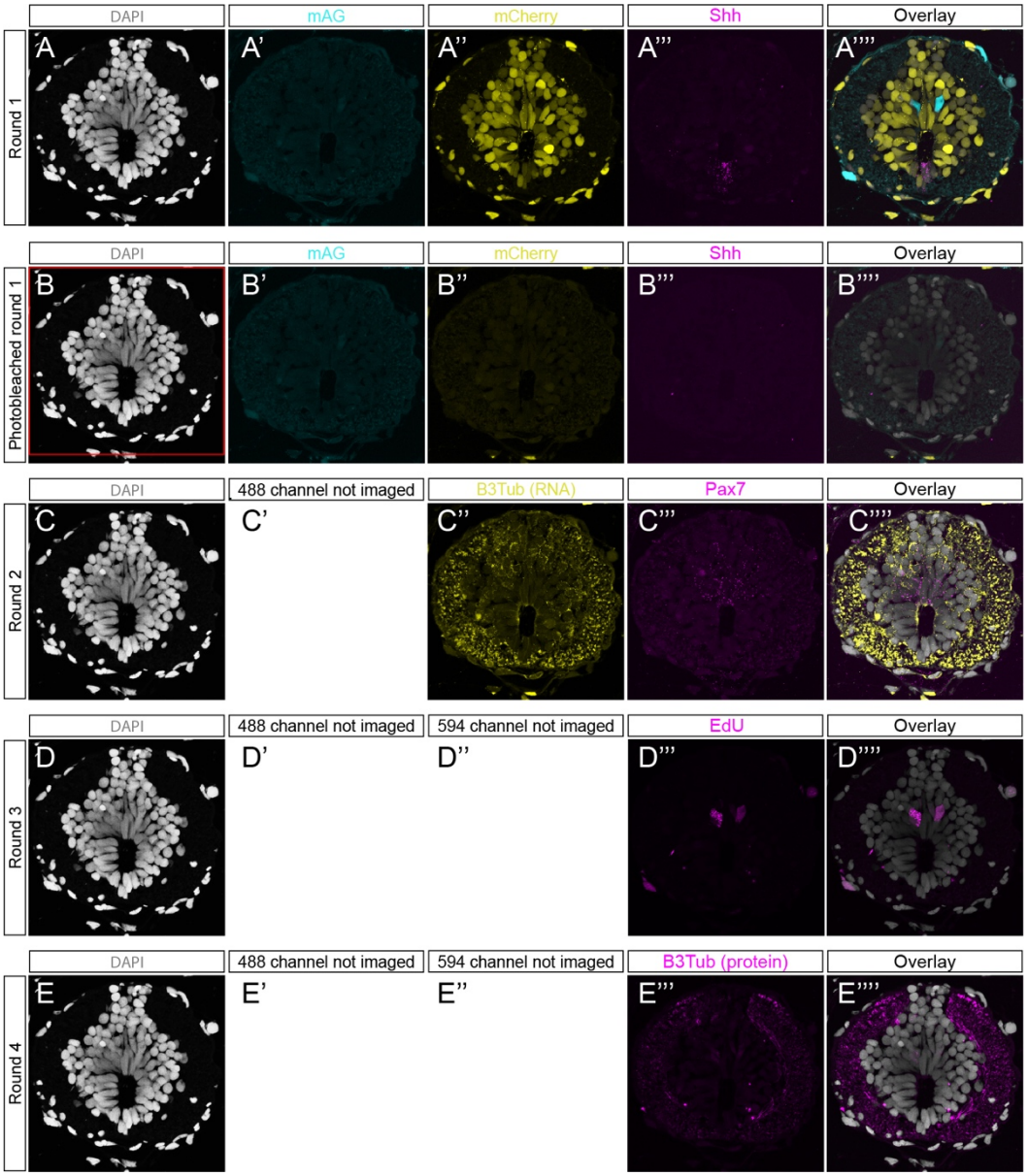

Fig. S5. Single channel images from Figure 4

(A-E'''') Individual channels from each round of multimodal imaging. Scale bar= 50 μm.

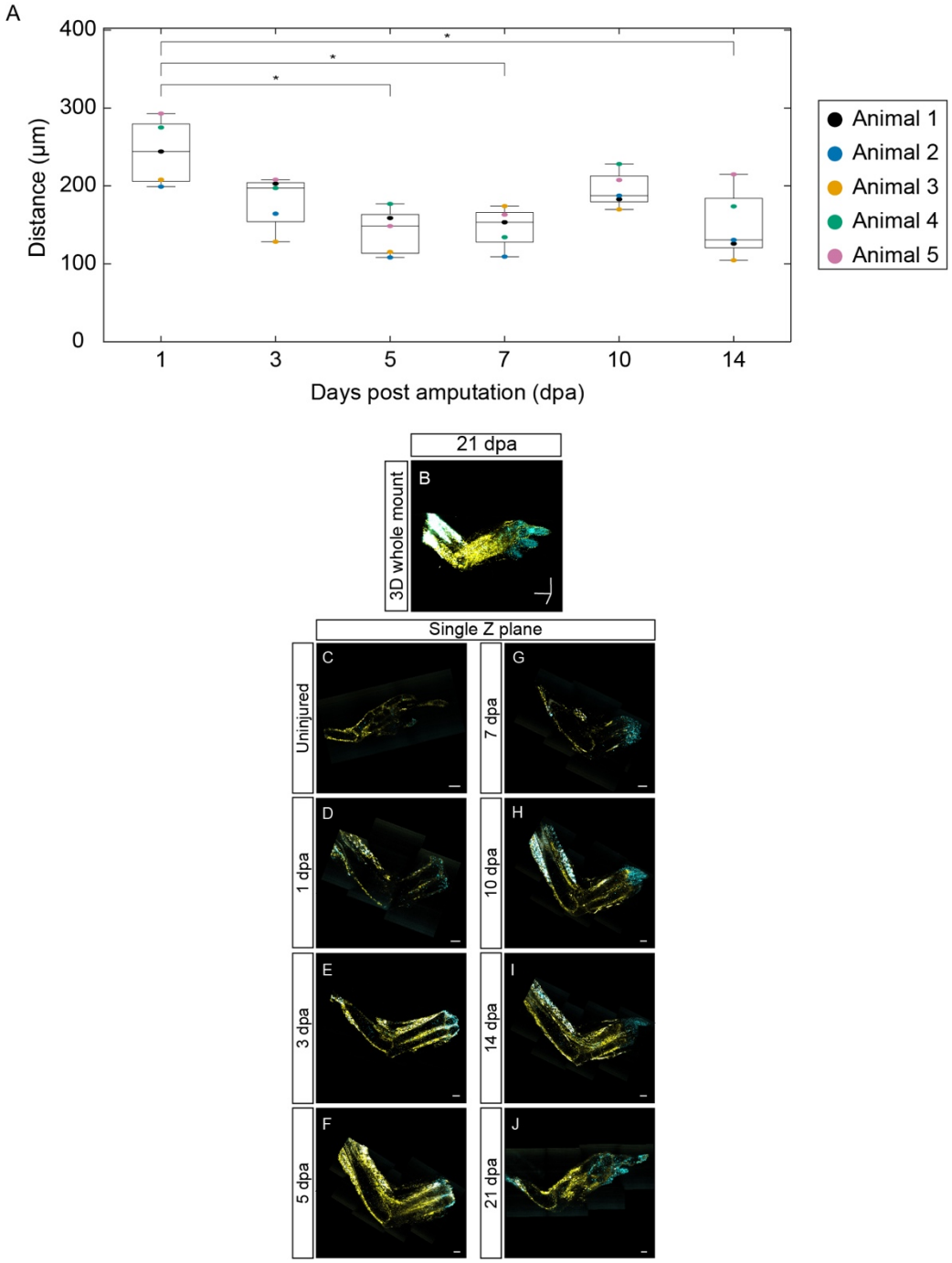

Fig. S6. Additional FUCCI limb regeneration information

(A) Quantification of the distance mAG fluorescence is observed from the amputation plane to the mCherry^{+} muscle line at each time point. Each dot color represents a replicate from a different animal. *= p-value < 0.05 (One-way ANOVA with a Tukey-Kramer multiple comparison test). (B) 3D, whole-mount image of 21 dpa FUCCI limb taken with light-sheet fluorescence microscopy. Scale bars= 600 μm in each axis. (C-J) 2D z-slices of whole-mount images from Fig. 5H-N and Fig. S6B. Scale bars= 200 μm.

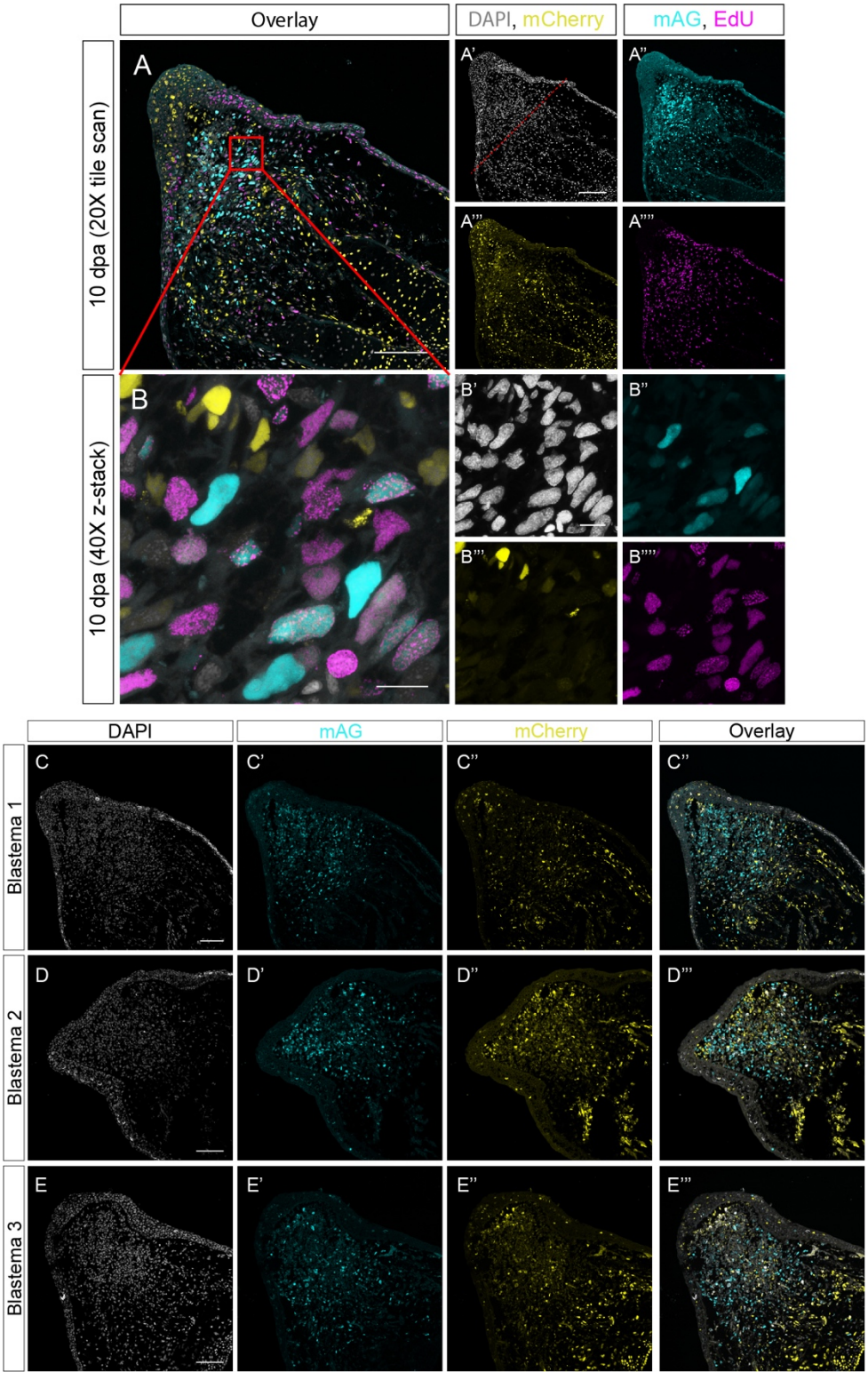

Fig. S7. Regenerating FUCCI limbs tissue sections

(A-A’’’’) 20X tile scan of a 10 dpa FUCCI blastema pulsed with EdU for three hours. Scale bars= 150 μm. (B-B’’’’) 40X z-stack of the EdU pulsed blastema mesenchyme. Scale bars= 25 μm. (C-E’’’) Single color channels for three replicates of 14 dpa FUCCI limbs. Scale bars= 100 μm.

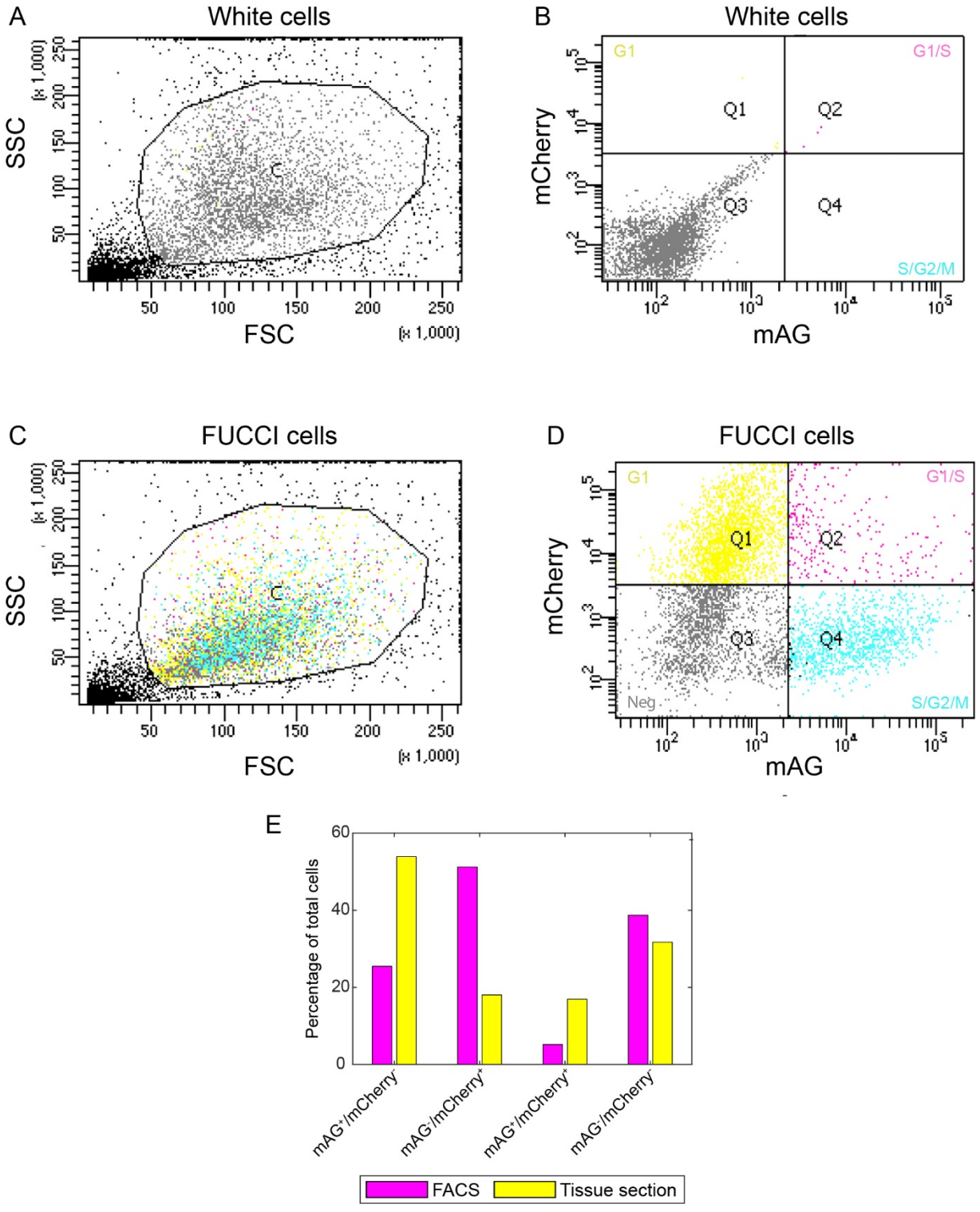

Fig. S8. Comparison between quantification in FACS and tissue sections

(A-D) Flow cytometry analysis of blastema cells from white strain (n=10, 4 cm animals aged 4 months) (A-B) and FUCCI (C-D) (n=10, 4 cm animals aged 4 months) axolotls. A forward scatter (FSC-A) and side scatter (SSC-A) plot was used to gate for the cell population (A, C). The stage of the cell cycle was determined using a FITC (mAG) versus PE-Texas Red (mCherry) scatter plot displaying only the gated cell population (B, D). Gates were established as described in methods. The cell population from the white blastema cells (A) represents 3,340 cells from a total of 10,000 events. Of these cells, 99.6% were included in the negative population and 0.2% fell in the red population (B). For the FUCCI blastemas, 5,682 cells were analyzed from the total 10,000 events (C). Of the cells, 32.1% were $mAG^-/mCherry^-$, 21.1% were $mAG^+/mCherry^-$, 42.5% were $mAG^-/mCherry^+$, and 4.3% were $mAG^+/mCherry^+$ (D). (E) Quantification of $mAG^+/mCherry^-$, $mAG^-/mCherry^+$, $mAG^+/mCherry^+$, and $mAG^-/mCherry^-$ cell populations in FACS sorted blastemas (n=10, 4 cm animals aged 4 months) and tissue sections (n=3, 7-8 cm animals aged 6 months).

Table S1. Crossing F1 FUCCI animals suggests the presence of multiple integrations

Cross	Number of offspring	FUCCI^{+}	FUCCI^{-}
F1 FUCCI male x d/d female	91	81 (89%)	10 (11%)
F1 FUCCI female x d/d male	26	22 (85%)	4 (15%)
F1 FUCCI x F1 FUCCI	263	251 (95%)	12 (5%)
F1 FUCCI x F1 FUCCI	132	132 (100%)	0 (0%)

Table S2. Number of animals and cells quantified at each anatomical position in Figure 6

AP location	Number of animals	Number of cells
-250 µm	4	157
-150 µm	4	156
Rod end	4	167
250 µm	4	203
500 µm	4	251
750 µm	4	283
1000 µm	4	276
5000 µm	4	514
Uninjured	5	540

Table S3. V3.HCR FISH probe sequences

Click here to download Table S3

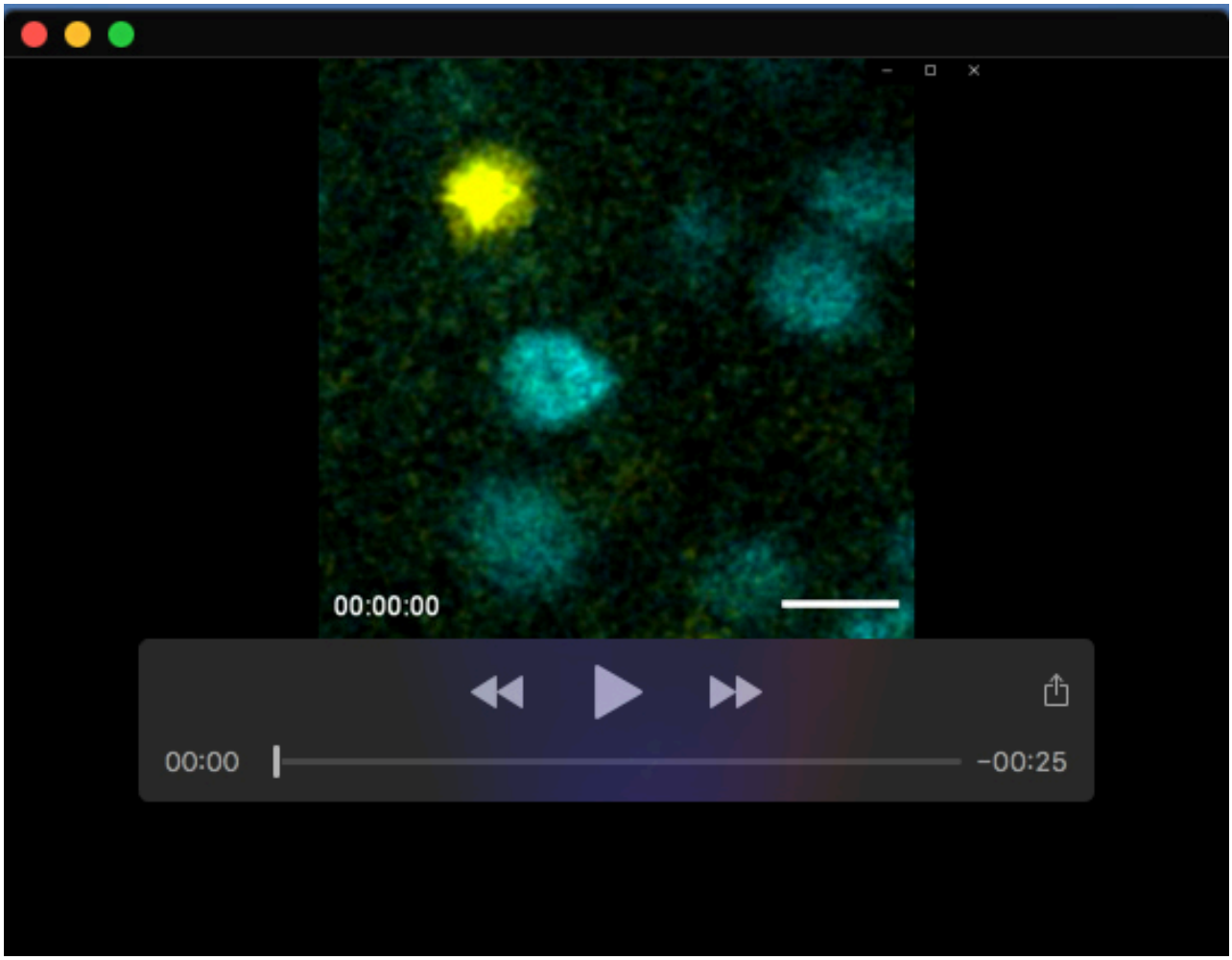

Movie 1. 16-hour live image of dividing epithelial cells in a stage 32 FUCCI larva
Scale bar = 100 μm.

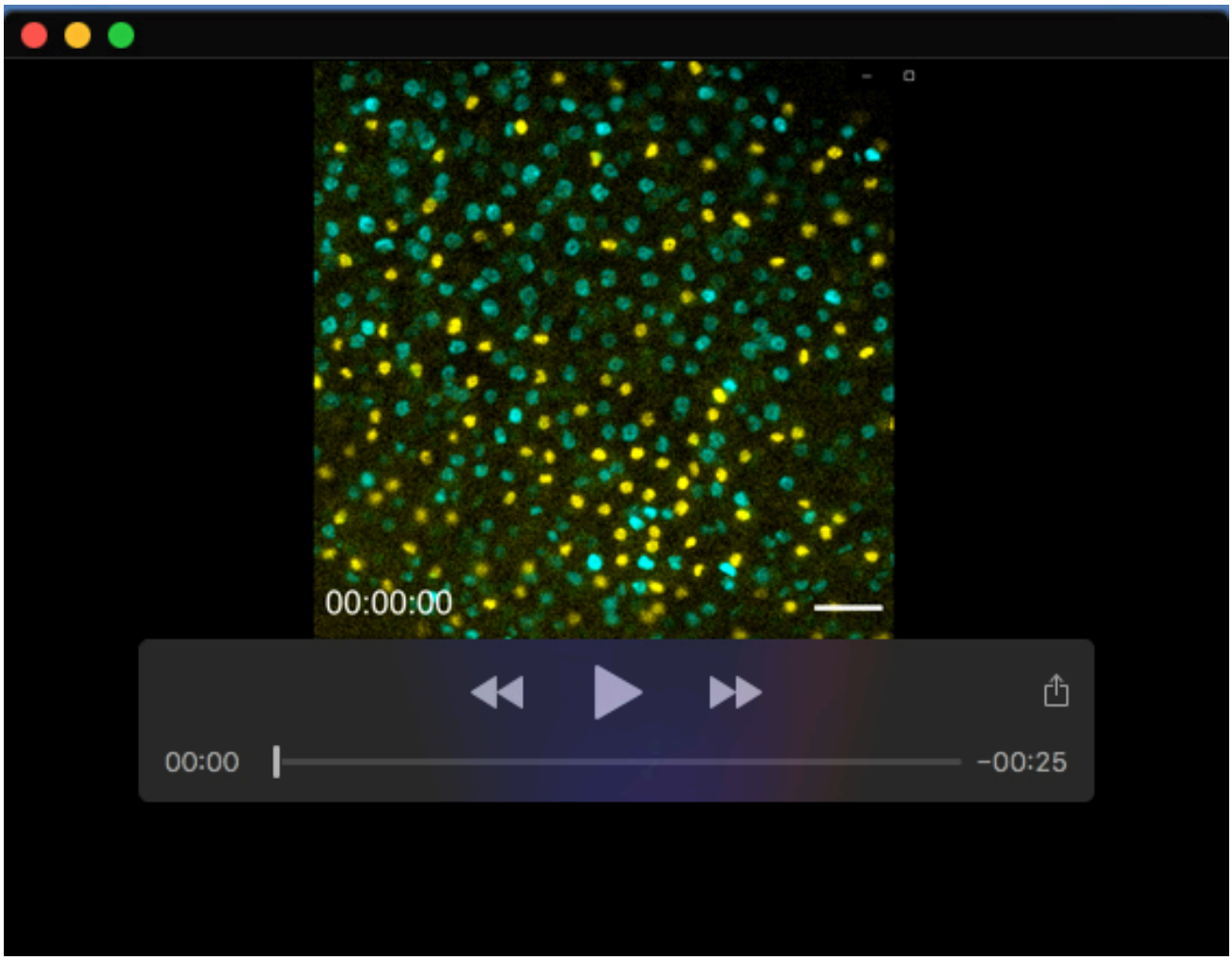

Movie 2. Dividing mAG+ epithelial cell from a stage 32 larva Scale bar= 25 μm.

Movie 3. 60-hour live image of tail regeneration from a stage 36 FUCCI larva
Animal mounted in 0.3% agarose immediately after amputation. Scale bar= 50 μm.

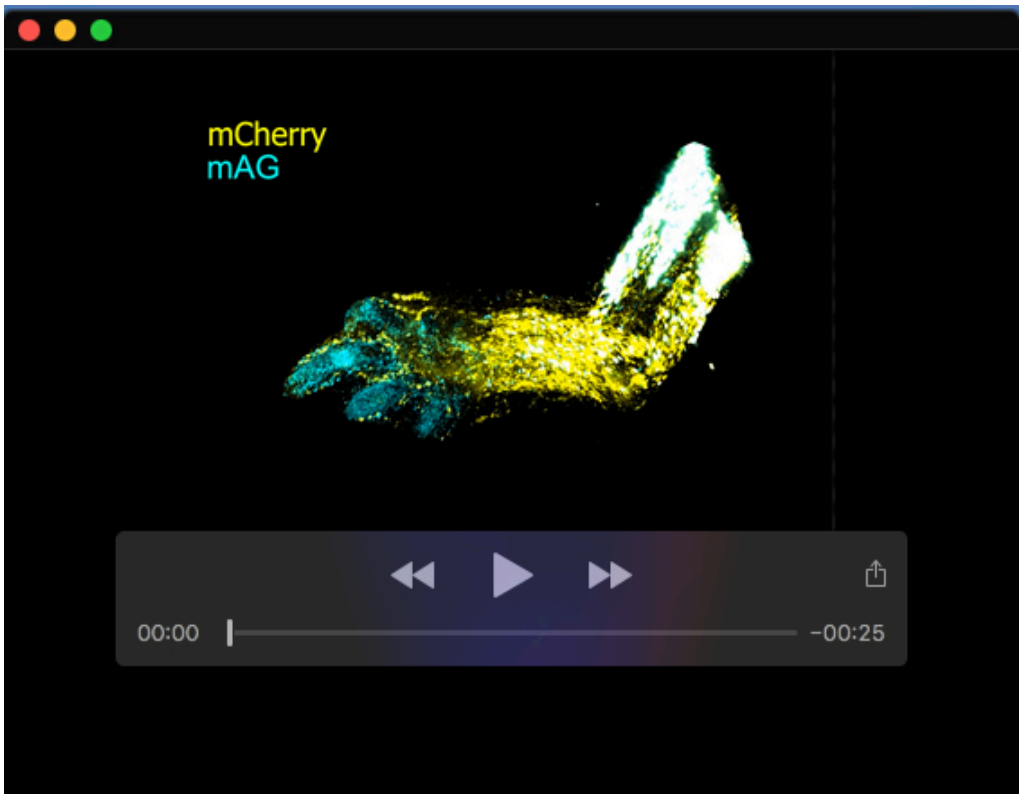

Movie 4. mAG tracks for each frame from Movie 3
Animal mounted in 0.3% agarose immediately after amputation. Scale bar= 50 µm.

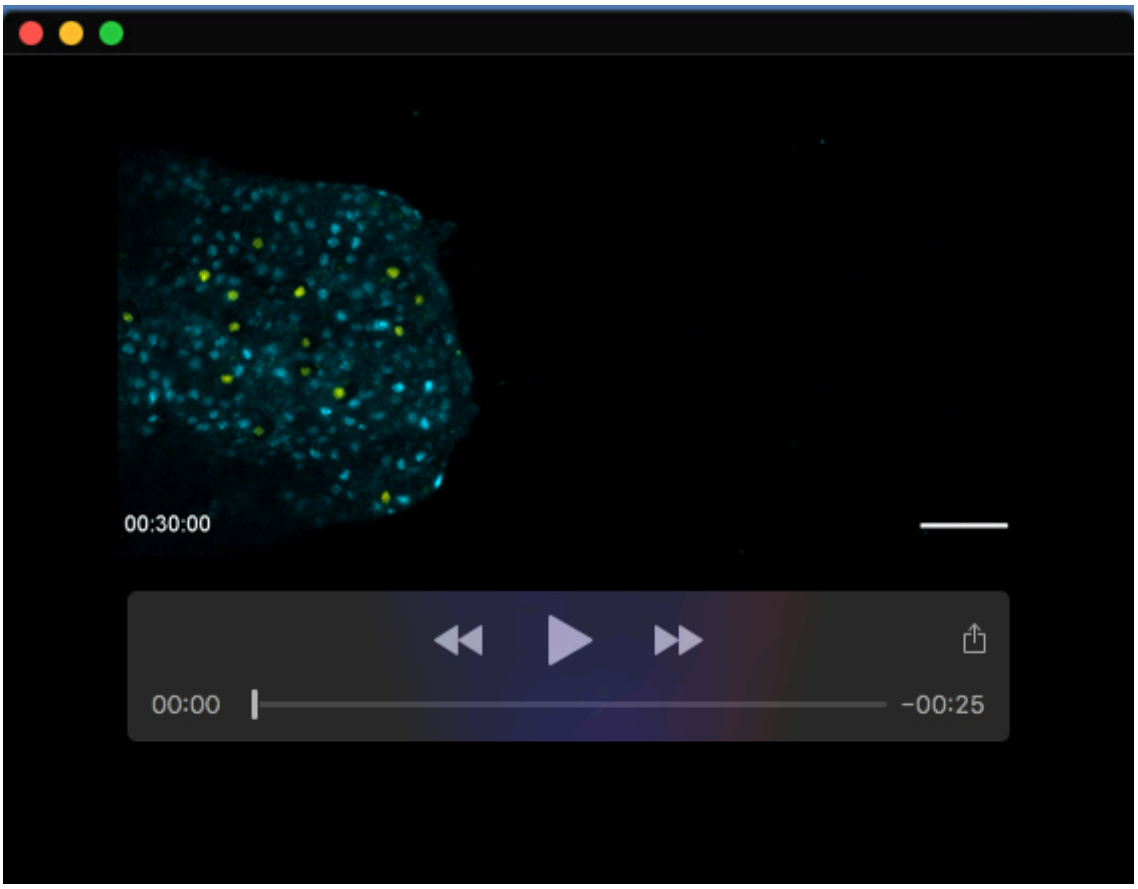

Movie 5. Whole-mount uninjured FUCCI limb.

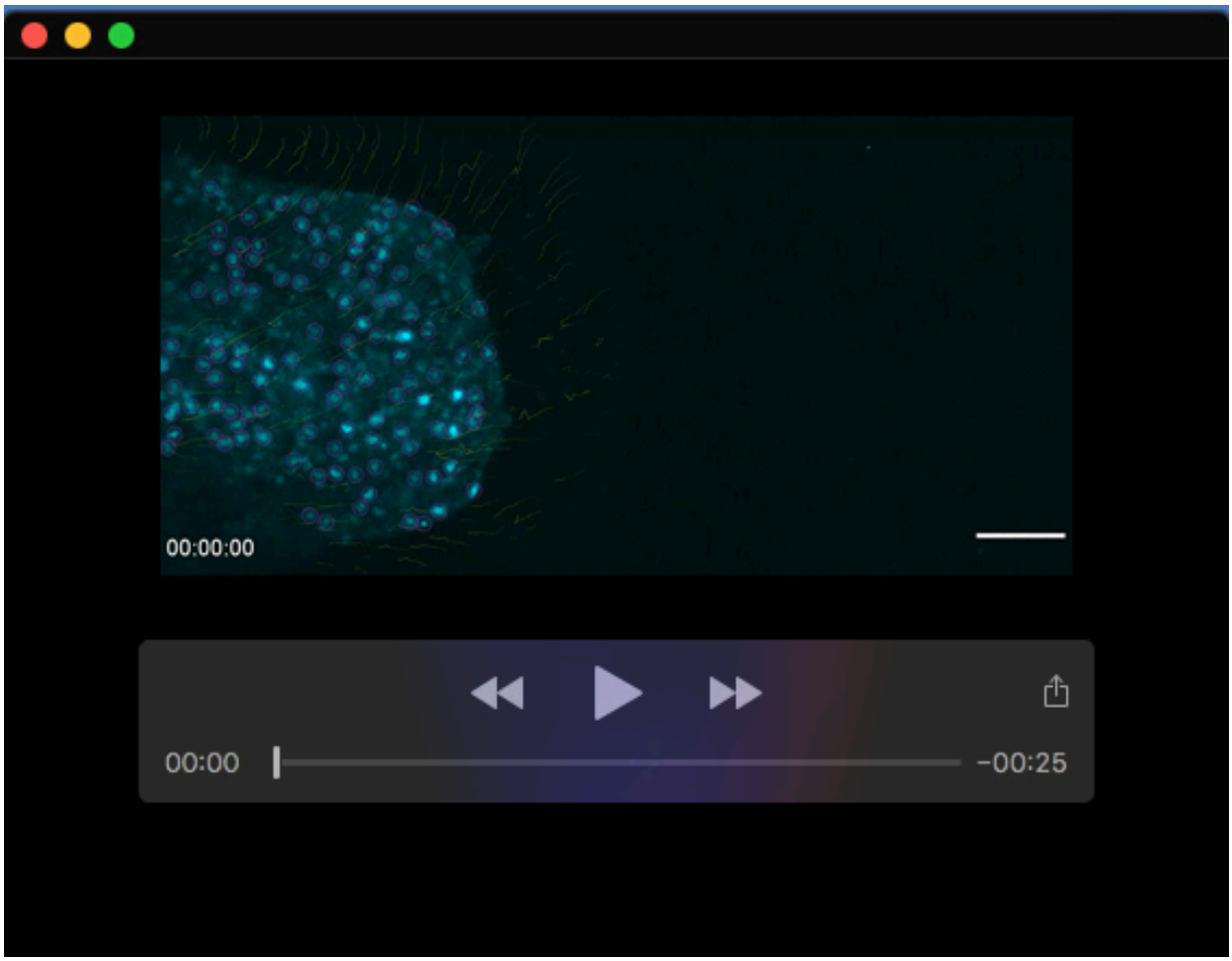

Movie 6. Whole-mount 21 dpa regenerating FUCCI limb.